Document Version
Final published version

Citation (APA)
Aşıkoğlu, A., Vasconcelos, G., Barontini, A., & Lourenço, P. B. (2025). Quasi-static test on half-scale modern unreinforced masonry building with plan irregularity. *Bulletin of Earthquake Engineering*, *23*(14), 6393-6435. https://doi.org/10.1007/s10518-025-02275-x

Bulletin of Earthquake Engineering
https://doi.org/10.1007/s10518-025-02275-x

ORIGINAL ARTICLE

Quasi-static test on half-scale modern unreinforced masonry building with plan irregularity

Abide Aşıkoğlu[1] · **Graça Vasconcelos**[2] · **Alberto Barontini**[2] ·
Paulo B. Lourenço[2]

Received: 28 March 2025 / Accepted: 27 August 2025

Abstract

Unreinforced masonry structures are a significant percentage of the global building stock and are often vulnerable to seismic events due to their inherent structural weaknesses and limited deformation capacity. Although seismic codes promote regularity in structural design, achieving this in unreinforced masonry buildings is often a challenging task. Despite extensive research using shake table tests, quasi-static testing of unreinforced masonry buildings remains limited, particularly in the presence of plan irregularity and rigid diaphragm. The present study addresses this research gap by investigating the seismic response of a half-scale, two-story, unreinforced masonry building with plan irregularity through cyclic quasi-static testing. The experimental campaign presented here shows the findings from two tests, including dynamic identification. The first test indicated torsional amplification and rocking-induced wall detachment during the pre-peak response. These results prompted modifications to the experimental setup, including the addition of extra weight to prevent overall rocking and the repairing of the boundary interface to re-establish structural integrity for subsequent testing. The initial results highlight the influence of plan irregularity within the pre-peak behaviour and provide a basis for further exploration in the seismic assessment of irregular, unreinforced masonry buildings.

Keywords Modern unreinforced masonry · Plan irregularity · Diaphragmatic action · Experimental analysis · Seismic performance · Quasi-static test

1 Introduction

The prevalence of unreinforced masonry (URM) buildings declined with advancements in reinforced concrete (RC) and steel structures. However, URM remains a sustainable and practical choice in certain regions. In low-seismic countries such as the United Kingdom,

---

✉ Abide Aşıkoğlu
a.ashikoglu@tudelft.nl

[1] Faculty of Civil Engineering & Geosciences, Department 3MD, Delft University of Technology, Delft, The Netherlands

[2] Department of Civil Engineering, University of Minho, ISISE, ARISE, Guimarães, Portugal

Germany, Switzerland, Slovenia, the Netherlands, and Brazil, it continues to be used for low- and mid-rise buildings (Beyer et al. 2015; Esposito et al. 2019; Triller et al. 2019; Lourenço and Marques 2020). In developing countries, including Nepal, India, Pakistan, Myanmar, and Algeria, URM construction remains prevalent, driven by socio-economic factors such as affordability, availability of traditional materials, and cultural familiarity with masonry techniques (Singh et al. 2013; Athmani et al. 2015; Brando et al. 2017; Gautam et al. 2018; Halder et al. 2020; Adhikari and D'Ayala 2020; Giordano et al. 2021; Bothara et al. 2022; Debnath et al. 2022; Aung et al. 2025; Imtiaz et al. 2025). Historically, masonry structures relied on craftsmanship and rule-of-thumb methods, often without adhering to seismic design codes. Nevertheless, several masonry building typologies around the world have demonstrated exceptional performance during major earthquakes (Ali et al. 2017; Bothara et al. 2022; Mercimek 2023).

Structural irregularity is one of the critical factors in seismic vulnerability, as it can lead to uneven force distribution, torsional effects, and localised failure mechanisms. European seismic design codes (EN 1998- 1:2004) encourage simple and box-like masonry buildings to ensure regularity; however, practical challenges arise. For instance, spatial limitations, economic factors, and the need to accommodate architectural demands often lead to structural irregularities, such as re-entrant corners, setbacks, asymmetric geometry, or non-uniform mass or stiffness distribution.

Seismic design codes classify structures as regular or irregular, with irregularities defined as either in plan or elevation based on geometry, distribution of the mass, stiffness, and strength. However, these criteria often fail to capture the inherent complexity of irregularities in masonry buildings. While some indices have been developed to quantify irregularities in URM buildings, they are mainly applicable to existing URM with flexible diaphragms, which often lack box behaviour, causing masonry walls to behave as individual façades (Parisi and Augenti 2013; Berti et al. 2017). Aşıkoğlu et al. (2021) highlighted the significant variation in how researchers interpret irregularity in masonry structures. For example, some studies attribute in-plan irregularities to wall and door opening distributions that could indirectly impose eccentricity, while others associate irregularities with setbacks or asymmetrically located wall configurations. Nevertheless, buildings classified as regular by a code can still exhibit irregular load paths that may prevent pure translational deformation and result in considerable torsional effects as damage progresses (Lourenço et al. 2013). Understanding the progression of the damage may give clues on how, or if, stiffness and forces will be redistributed in ways that lead to torsional effects. This raises questions about the well-established assumptions on box behaviour, which only consider in-plane mechanisms and neglect the role of out-of-plane walls or the flange effect, especially after the progression of nonlinear deformations. Additionally, material variability across the building, such as inconsistencies in masonry unit properties, mortar quality, and workmanship, can also contribute to structural irregularities.

Understanding the influence of structural irregularities on the response of URM buildings requires a comprehensive approach that integrates both numerical and experimental analyses. Experimental campaigns provide a robust basis for refining numerical analyses, enabling extrapolated responses to scenarios and parameters that may not be feasible to investigate experimentally. However, these studies face significant challenges, including high costs, limited test models, equipment, time, and expertise. Dynamic shake-table tests have been extensively carried out, while the number of comprehensive studies on cyclic quasi-static testing on URM buildings remains limited. Notably, Haindl et al. (2024) compiled data from 69 shake-table tests on URM buildings and provided them in an open-access database. These campaigns focused on the seismic response of historical and existing masonry structures, where the absence of a rigid diaphragm often results in a localised failure mechanism. Plan irregularity was investigated by only a few studies, such as Bairrão and Silva (2009); Avila et al. (2018); Kallioras et al. (2018). Nevertheless, shake-table instruments are rarely available in most laboratories due to their complexity and cost. In contrast, quasi-static testing is more commonly implemented for component-level experiments, such as walls, piers, or spandrels. However, the ability to test multi-storey structures is often constrained by the absence of essential infrastructure like reaction walls and slabs, as well as advanced control systems. Shake table testing remains a preferred method in seismic research because it can replicate real ground motion records and capture dynamic structural responses. Moreover, inertial and gravitational forces are inherently present, which govern the structural behaviour during dynamic loading. Quasi-static testing, on the other hand, requires more elaborate setups to simulate representative lateral loads, and the selection of load pattern, such as mass-proportional or uniform distributions, involves assumptions that may simplify actual seismic demand. Despite these challenges, quasi-static testing offered a practical compromise for the present study. The key structural behaviour was investigated under controlled conditions with sufficient accuracy and repeatability, while making efficient use of available laboratory resources.

A summarised literature review on the quasi-static tests performed on URM buildings is presented in Table 1. Experimental campaigns have primarily studied regular structures at a full scale (1:1) with varying material properties, diaphragm types, typology, and loading conditions. Several studies focus on existing URM typologies with flexible timber diaphragms (Magenes et al. 1995; Yi et al. 2006; Gattesco et al. 2023). Others examine URM buildings with RC diaphragms, which can be found in both existing (Shahzada et al. 2012; Aldemir et al. 2017, 2018) and modern structures (Chourasia et al. 2016; Esposito et al. 2019; Triller et al. 2019). The number of models (N_M) per study is generally limited, with most research relying on a single model. The current state of the art includes experimental models with regular configurations, and there is no documented quasi-static test on URM buildings focusing on structural irregularities, particularly in plan setbacks. Based on these observations, various research gaps that remained unexplored experimentally within the scope of URM buildings with irregularity are identified, namely: (i) the influence of plan irregularities, such as setbacks, diaphragm openings, or the presence of structural masonry partition walls; (ii) the impact of different opening sizes and their distribution on the walls or façades on both overall and local responses; and (iii) the effect of eccentricities between centres of mass and rigidity across floors.

The present research addresses gaps in the literature through an experimental campaign on modern URM buildings with plan irregularity. In this paper, the term *modern URM buildings* refers to unreinforced masonry constructed using recent materials, such as reinforced concrete and contemporary masonry units, and designed in accordance with current seismic codes, with adequate wall-to-wall and wall-to-floor connections to ensure rigid diaphragm behaviour. The study focuses on quasi-static testing and evaluates the influence of plan irregularity on global seismic response. The research aimed to generate experimental data to support and facilitate numerical studies, as well as to assess the building's performance. Within this framework, cyclic quasi-static tests were conducted on a half-scale, two-

Table 1 List of quasi-static tests available in the literature, including their structural configuration and test characteristics

Experimental Model		Material	Scale	Diaphragm	N_S	Loading	N_M
(Magenes et al. 1995)	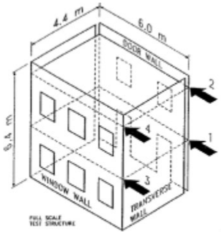	Solid clay brick; Lime-based mortar **Typology**: Existing	1:1	Flexible; Timber	2	Two-way cyclic; Displacement-control; Uniform load pattern; Uniaxial	1
(Yi et al. 2006)	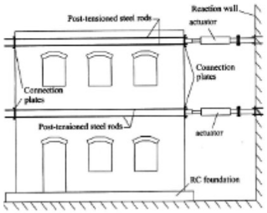	Solid and core clay bricks; Low-strength cement-based mortar **Typology**: Existing	1:1	Flexible; Timber	2	Two-way cyclic; Displacement-control; 1st mode proportional load pattern; Uncoupled uniaxial	1
(Shahzada et al. 2012)	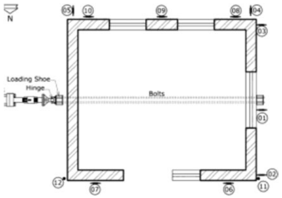	Clay **Typology**: Classified as existing by the authors to represent an old URM with RC slab.	1:1	Rigid; RC	1	Two-way cyclic; Displacement-control;	1

Table 1 (continued)

Experimental Model		Material	Scale	Diaphragm	N_S	Loading	N_M
(Chourasia et al. 2016)		Solid clay brick; Cement-based mortar **Typology**: Modern	1:1	Rigid; RC	1	Two-way cyclic; Displacement-control; Uniaxial	1
(Aldemir et al. 2017)		Vertical perforated clay brick; Mortar N.A. **Typology**: Existing	1:1	Rigid; RC	2	One-way cyclic; Displacement-control; Triangular load pattern; Uniaxial	1
Aldemir et al. (2018)	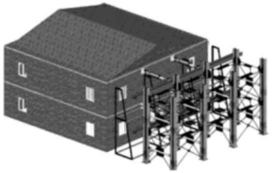	Solid clay brick; Cement-based mortar **Typology**: Existing	1:1	Rigid; RC	2	One-way cyclic; Displacement-control; 1st mode proportional load pattern; Uniaxial	1
(Esposito et al. (2019)	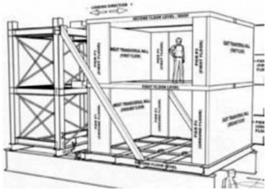	Calcium silicate brick; Cement-based mortar **Typology**: Modern	1:1	Rigid; RC	2	Two-way cyclic; Displacement-control; Mass proportional (uniform) load pattern; Uniaxial	1

Table 1 (continued)

Experimental Model		Material	Scale	Diaphragm	N_S	Loading	N_M
(Triller et al. 2019)	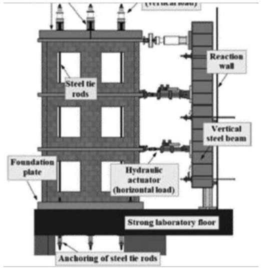	Vertical perforated clay brick; Cement-based mortar **Typology**: Modern	1:1	Rigid; RC	3	Two-way cyclic; Displacement-control; Inverse triangle load pattern; Uniaxial	1
(Choudhury and Kaushik 2021)	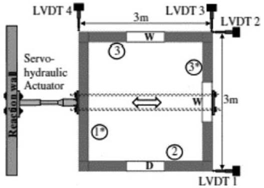	Solid clay brick; Cement-based mortar **Typology**: Not specified by the authors, but the response may fall into box-behaviour.	1:1	Rigid; RC	1	Two-way cyclic; Displacement-control; Uniaxial	1
(Gattesco et al. 2023)	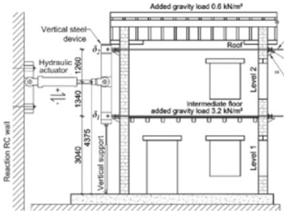	Rubble stone; Lime-based mortar **Typology**: Existing	1:1	Flexible; Timber	2	Two-way cyclic; Displacement control; No pre-defined load pattern; Uniaxial	1

story modern URM building with plan irregularity. A representative structural layout was selected based on the literature, and the structural irregularity was introduced by a setback in one corner of the building plan. The results highlight the influence of plan irregularity on pre-peak behaviour and provide a basis for further exploration in the seismic assessment of irregular URM buildings.

2 Description of the experimental campaign

The experimental campaign was composed of two parts: (i) material characterisation tests and (ii) quasi-static cyclic structural tests. In the first phase, material characterisation tests were performed to obtain the key mechanical properties of the materials selected for construction, as detailed in Aşıkoğlu (2024). The second phase aimed to evaluate the seismic behaviour of a URM building with in-plan irregularity through cyclic quasi-static testing and ambient vibration measurements. Initially, the test was designed to assess the as-built structure, with the first test (Test 1) providing baseline data on its performance. Following the results of Test 1, it became clear that modifications were necessary to continue testing. As a result, the boundary interfaces of the masonry walls were repaired, and additional weight was added, facilitating the execution of the second test (Test 2).

2.1 Building model

The experimental building was designed to represent the distinctive features of typical residential Portuguese houses, which often exhibit in-plan irregularities, namely a setback on one side (Avila et al. 2018). The building is a standalone structure without adjoining buildings, as shown in Fig. 1. The south façade does not have any openings, considering a design that would allow for the attachment of an adjoining building, thereby creating a semi-detached house. The scaled structure was designed following Eurocode principles and assessed using a performance-based approach. A behaviour factor (q factor) was not applied, as the evaluation focused on deformation, damage, and energy dissipation. The selected configuration corresponds to a two-story residential building in the Lisbon area. It was designed for a peak ground acceleration of 0.15 g on rock ground conditions (Ground

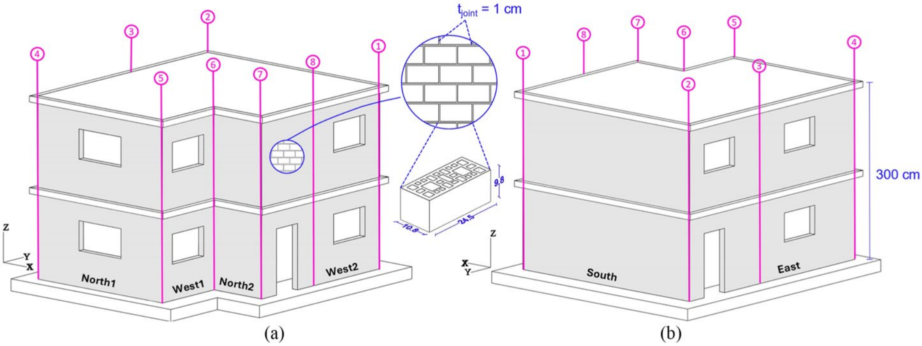

Fig. 1 Three-dimensional representation of the experimental building: (**a**) North-West façades, (**b**) South-East façades. (Units are in cm)

Type A), considering Type 1 seismic action, which is characterised by a spectral shape shifted toward the longer periods, typically associated with surface-wave magnitude (M_S) greater than 5.5 (EN 1998-1:2004; Bisch et al. 2012).

The experimental building was designed and constructed at a half-scale to accommodate the spatial constraints of the reaction wall and floor while optimising available resources at the Structures Laboratory of the University of Minho. The experimental model was a two-story unreinforced masonry (URM) building with an inter-story height of 150 cm and a rigid diaphragm, featuring an RC slab for each floor. The plan layout of the building had dimensions of 419 cm x 368 cm, as illustrated in Fig. 2. Key structural features, such as the dimensions of the walls, windows and door openings, were scaled. For detailed geometric aspects of the building, refer to (Aşıkoğlu 2024).

To ensure that the results obtained from the model would be meaningfully interpreted and extrapolated to the full-scale structure, a consistent scaling methodology was adopted based on principles applicable to static testing. Unlike dynamic testing, where inertial forces play a significant role and similitude laws, such as Cauchy or Froude, are applied, the structural response in quasi-static testing is governed by equilibrium conditions with negligible inertial effects. Therefore, the scaling approach focused on preserving the relationships between geometry, material properties, and mechanical response under static equilibrium. As shown in Table 2, only geometric scaling factor λ_G was applied, and all linear dimensions of the model (length, height, thickness) were scaled. Material properties such as Young's modulus and density were assumed to be the same. Consequently, derived quantities such as area, volume, and mass were scaled accordingly based on the geometric scale factor of 1:2.

Commercial bricks were selected considering the same scale factor to account for an accurate simulation of geometry and stress-strain relationship, considering five main criteria: (i) compressive strength higher than 10 MPa; (ii) dimensions compatible with the scaled geometry (1:2); (iii) similarity to full-scale units; (iv) clay masonry material; (v) vertical perforated unit. A vertical perforated clay brick unit with dimensions of 24.5 cm x 10.8 cm x 9.8 cm (length x width x height) was selected, as seen in Fig. 1. The unit dimensions of these

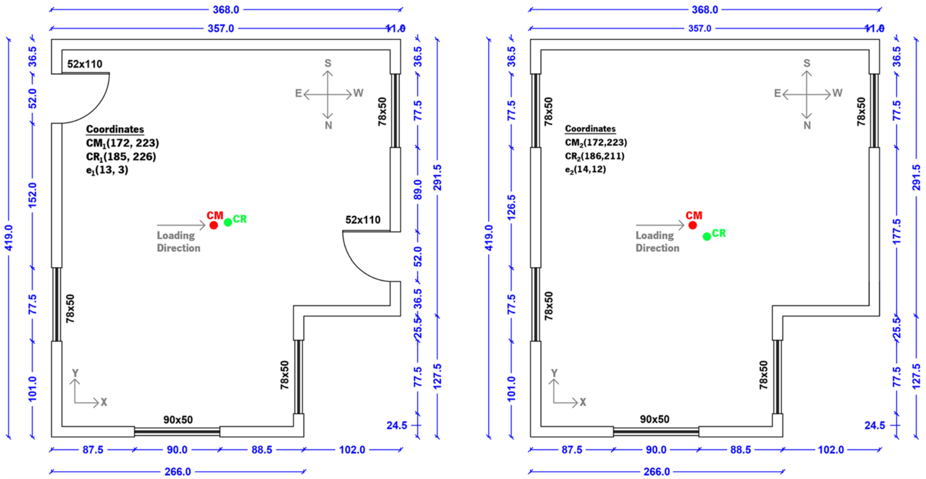

(a) (b)

Fig. 2 Plan dimensions of the experimental building: (**a**) first floor, (**b**) second floor (Units are in cm)

Table 2 Summary of geometric scaling used in the quasi-static test campaign

Parameter	Scaling Factor	Description
Length (L)	λ_G	Geometric scaling of dimensions
Height (H)	λ_G	Geometric scaling of dimensions
Thickness (t)	λ_G	Geometric scaling of dimensions
Area (A)	λ_G^2	Derived from length scaling
Volume (V)	λ_G^3	Volume scales with the cube of length
Young's Modulus (E)	1	Material property is assumed to be the same
Density (ρ)	1	Material property is assumed to be the same
Mass (M)	λ_G^3	Mass scales with volume for the same material

bricks were slightly larger than those required by the 1:2 scale factor. As per (EN 1996-1-1:2005, 2005), the selected clay brick falls under Group 3, having a compressive strength of at least 15 MPa. A running bond masonry pattern was adopted, ensuring the interlocking of the intersecting orthogonal walls to enhance structural coherence. A cement-based mortar with a compressive strength of 10 MPa (M10 commercial mortar mix) was considered for masonry wall construction. The same mortar was used for the first course over the beam foundation and RC slab on the second floor.

Concerning the regularity definitions outlined in the seismic design codes, such as (EN 1998-1:2004, 2004; ASCE/SEI 7–16 2017; NTC 2018; TBSC 2019), the indices for plan irregularities, including torsion, setbacks, and plan slenderness, were calculated per each code's specific criteria, as presented in Table 3. The values obtained exceed the respective thresholds, confirming that the experimental building exhibits plan irregularity, which includes torsion and setback.

2.2 Test setup

The test setup included two actuators aligned with the centre of mass (CM) on each floor to apply the lateral load. Each actuator had a maximum force capacity of 300 kN with a displacement range of ± 200 mm. Data were acquired at a rate of four points per second. Unidirectional loading was applied to the building in the transversal (X) direction, where plan irregularity was expected to have a greater impact than its longitudinal (Y) counterpart due to the calculated eccentricity (Fig. 2). This behaviour was later confirmed through dynamic identification. The specific configuration of the actuators was designed strategically to meet two primary objectives: (i) distribute the load across the slab to avoid point load application, and (ii) facilitate load application in both positive and negative directions, as well as load release, particularly after damage formation. The first objective was accomplished by mounting steel profiles along the perimeter of the building, as shown in Fig. 3. Each actuator was installed on a reaction wall, and the load application end of the actuator was connected to the steel profiles through plates, referred to as loading plates (Fig. 4). Three-dimensional hinges were connected at both ends of the actuators, allowing the system to rotate.

As the reaction wall was L-shaped, the reverse loading was applied through the same actuator (pull). To apply push and pull forces, post-tensioned rebars were placed within the slab, passing across the parallel walls. The use of post-tensioned bars with a diameter

Table 3 Quantification of plan irregularity according to various seismic codes and their respective regularity limit

Irregularity Type	Experimental Building	(EN 1998-1:2004, 2004)	(TBSC 2019)	(ASCE/SEI 7–16 2017)	(NTC 2018)
Torsion 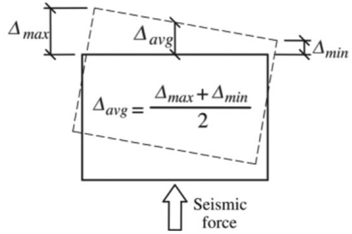	$\frac{\Delta_{max}}{\Delta_{avg}} = 1.3$	N/A	$\frac{\Delta_{max}}{\Delta_{avg}} > 1.2$	*Irregular*: $\frac{\Delta_{max}}{\Delta_{avg}} > 1.2$ *Extreme*: $\frac{\Delta_{max}}{\Delta_{avg}} > 1.4$	N/A
Setback 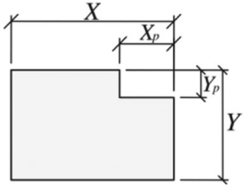	0.07[a] 0.28 (X)[b] 0.30 (Y)[b]	$\frac{A_{set}}{A_{plan}} > 0.05$	$\frac{X_p}{X} > 0.20$ $\frac{Y_p}{Y} > 0.20$	$\frac{X_p}{X} > 0.15$ $\frac{Y_p}{Y} > 0.15$	$\frac{A_{set}}{A_{plan}} > 0.05$
Plan Slenderness* $\frac{L_{max}}{L_{min}}$ L_{max}: Maximum plan dimension L_{min}: Minimum plan dimension	1.14	>4.00	N/A	N/A	>4.00

a: EN 1998-1:2004; 2004), NTC (2018)

b: TBSC (2019), ASCE/SEI 7–16

X: Transverse direction of the building

Y: Longitudinal direction of the building

N/A: Not applicable

* The term "plan slenderness" in the codes refers to the ratio between the max and min plan dimensions

of 20 mm within the RC slab is an important feature of this experimental campaign. As these bars were unbonded, they were considered non-structural elements. Indeed, the post-tensioned rebars were placed inside PVC tubes with a diameter of 24 mm to avoid being cast with concrete and to provide free movement before the post-tensioning (Fig. 5(a)).

Loading plates were used to ensure the integrity of the steel profiles under pullover and pushover forces. Furthermore, it was crucial to prevent the detachment of the profiles from the slab, allowing them to distribute the load uniformly. The loading plates, fixed to the actuators, were linked to so-called reloading plates via these post-tensioned rebars, as shown in Figs. 4 and 5(b) and (c). This method enabled the efficient transfer of reverse load from the actuator to the reloading plate via an interconnected bar during the pulling phase.

With the actuators configured, Linear Variable Differential Transformers (LVDTs) were deployed at various locations throughout the building, enabling both local and global measurements, as shown in Fig. 6. A total of 39 LVDTs were strategically placed, allowing detailed tracking of deformation. These measurements were crucial for capturing the building's response throughout the test. By categorising the LVDTs into four groups, it was possible to monitor different deformation mechanisms for an in-depth analysis of (i) diagonal shear, (ii) lateral, (iii) uplift, and (iv) sliding deformations. It is important to note that LVDTs used to measure lateral displacement were placed on the last course of bricks in the masonry wall rather than being positioned directly on the RC slab. This decision was made due to steel profiles mounted along the perimeter of the RC slabs, which could create clearances at the interface between the slab and the profile.

The construction of the building was carried out directly in the testing area by the same workers throughout the construction to ensure consistency in quality. The reader is directed to Aşıkoğlu (2024) for the details of the construction, step-by-step descriptions of the components, and a static plan of the RC slab, foundation, and masonry walls. As part of the construction, lintels were placed above the openings, matching the height of a single masonry course. Lintels consisted of two steel rebars with a diameter of 8 mm embedded in a cement-based mortar. Above the masonry walls, ring beams were embedded in the RC slabs, having 4φ8 mm longitudinal reinforcement and φ8//300 mm stirrups. These ring beams provided connection and transmission of the forces between the structural walls and the slab (Fig. 7 (a) and (b)). The steel profiles representing the loading beams served as a formwork for the slab during the construction (Fig. 7 (c)). These profiles were assembled in situ, and their connection was provided through corner profiles, as shown in Fig. 7 (d). The construction was then followed by the placement of the flexural reinforcement along the two directions of the slab with φ8//150 mm. Finally, PVC tubes and the post-tensioned bars were installed. Thus, concrete was cast once the steel profiles were placed to ensure complete coverage of the interface between the RC slab and the loading beams.

The structural mass of the experimental building was determined, and a mass breakdown considering each structural component is provided in Table 4. The mass of each RC slab was found to be 3705 kg. It should be noted that the thickness of the slab was adjusted to 10.5 cm for the mass calculations, despite the design being carried out with a thickness of 10.0 cm. The main reason for this was that during the demolition of the structure, it was possible to measure the accurate thickness of the slabs, given that some deviations could be present during the in-situ casting (refer to Aşıkoğlu (2024)). Accordingly, the mass of the first and second floor slabs accounts for 60.4% of the total mass. On the other hand, 31.8% of the mass is attributed to the masonry walls. Due to slight differences in window and door

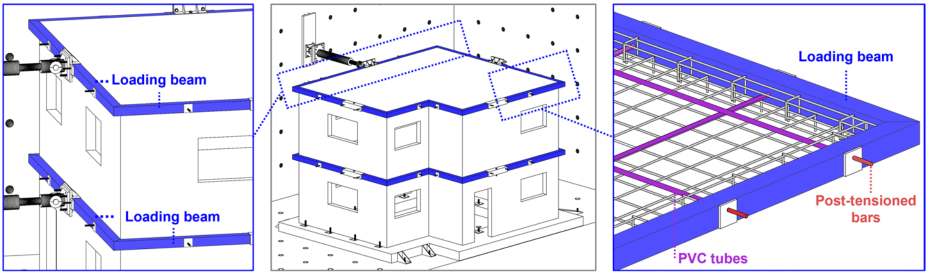

Fig. 3 A 3D visual representation of the experimental building with loading beams located along the perimeter of the building plan and post-tensioned bars within PVC tubes (shown in violet colour) and their connection to the loading beams

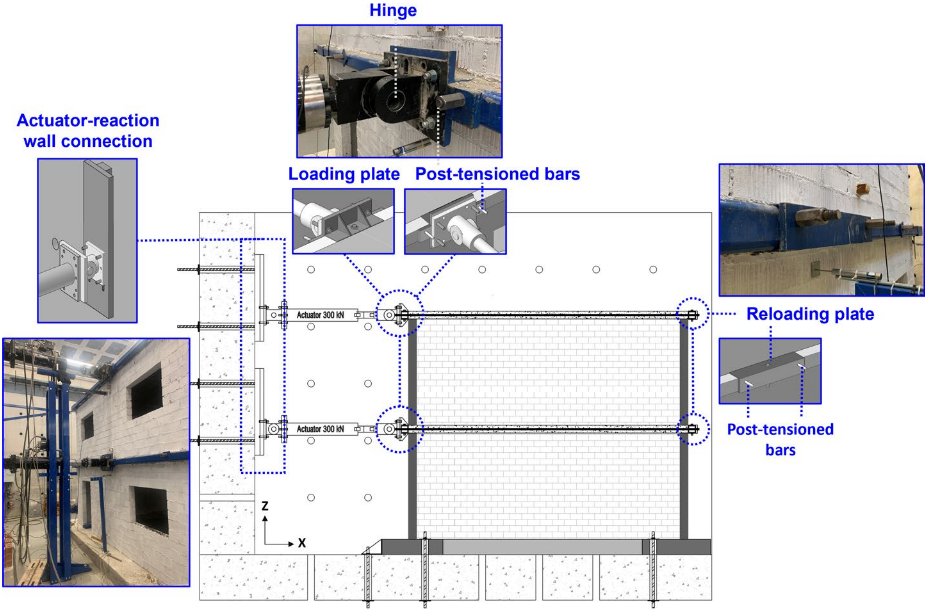

Fig. 4 Details and representation of the experimental setup at a cross-section along the centre of mass


(a) (b) (c)

Fig. 5 Details of the RC slab: (**a**) placement of PVC tubes, (**b**) connection of the post-tensioned bars to the loading plate, (**c**) connection of the post-tensioned bars to the reloading plate

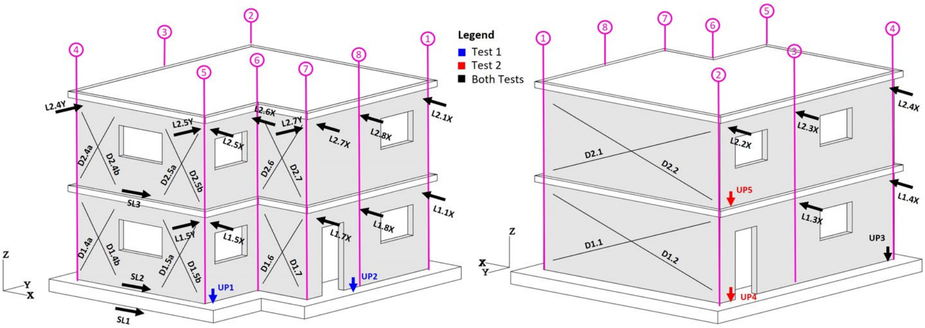

Fig. 6 LVDT configuration: (**a**) North-West façade, (**b**) South-East façade

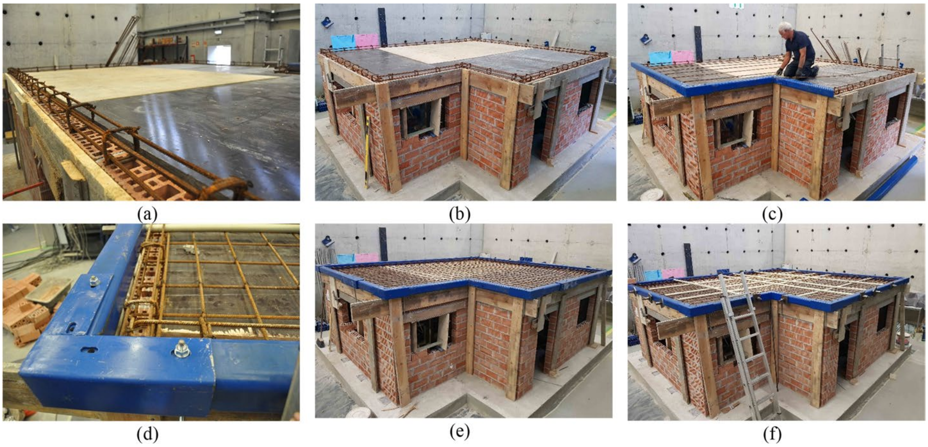

Fig. 7 Construction stages of the RC slab: (**a-b**) embedded ring beams in the RC slab, (**c-d-e**) reinforcement and loading beam assembly, (**f**) installation of PVC tubes and post-tensioned bars

Table 4 Mass breakdown of the experimental Building

Components	Density (kg/m³)	Mass (kg)	Percentage (%)
RC slabs (2 floors)	2500	7410	60.4
Masonry walls (first floor)	1651[‡]	1920	31.8
Masonry walls (second floor)		1990	
Steel profiles	8050	960	7.8
Total mass*		12,280	100
Foundation	2500	6850	-
Additional mass		1713	13.9[⁎]

* Total mass does not consider the mass of the foundation and additional mass

[‡] Value obtained from material characterisation

[⁎] Ratio of mass added to the structure with respect to structural mass (Additional mass/Total mass) openings, the mass of each masonry wall was calculated individually. The net volume of the brick units, which was equivalent to 53% of the gross volume, and the density of the brick obtained by the material characterisation test were considered for the mass calculation.

Although the steel profiles did not function as a structural element, their mass was taken into account for the overall mass calculations since their weight contributes to the self-weight and influences the base shear coefficient calculation. The steel profiles were determined to have a mass of approximately 960 kg, which accounts for 7.8% of the total mass. Finally, the total mass of the structure was calculated to be 12,280 kg (120.5 kN weight). It is important to note that the mass of the foundation was not relevant to the lateral strength of the structure. Therefore, its mass, 6850 kg, was disregarded from the total mass of the structure. With the construction complete, Fig. 8 presents an overview of the experimental building before testing. The black speckle pattern visible on the North-West façade was applied for Digital Image Correlation (DIC), which is not discussed in the current paper for conciseness.

As part of the experimental setup validation, sliding and overturning checks were performed to ensure the stability of the specimen under lateral loading. Sliding was assessed by verifying the capacity of the steel bars anchoring the foundation to the reaction floor based on the maximum expected shear force, and LVDT measurements, which are presented in the Results section, confirmed that no significant sliding occurred. For overturning, a simplified preliminary calculation was carried out by considering the structure as a rigid body to estimate the critical lateral load that would initiate cracking. Accordingly, there was no evidence of uplift between the foundation and the reaction slab during testing. However, rocking was observed at the base of the masonry walls, indicating that the assumptions made for preliminary calculation might have underestimated the response since they only accounted for translational response. Torsional effects might have influenced the actual overturning behaviour in the system. These effects could have locally reduced the stabilising moment at the base.

2.3 Modifications

Following the completion of Test 1, minor damage was observed on the structural walls. However, the boundary interface of the walls was detached from the foundation, leading to detachment at the base. To ensure the specimen remains suitable for continued testing, lim-

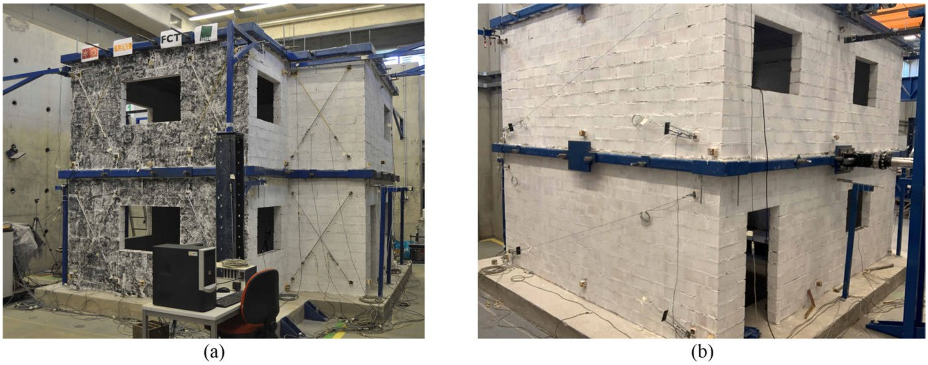
(a) (b)

Fig. 8 Experimental building: (**a**) North-West façade, (**b**) South-East façade ited modifications were carried out prior to Test 2. These modifications were guided by practical considerations and focused exclusively on restoring the original boundary conditions without altering the specimen's structural characteristics. Specifically, fluid mortar (Mape-Antique I) was used to re-establish the wall-foundation and wall-slab connections, ensuring continuity in load transfer and overall stability, see Table 4. The repair was carried out along the perimeter at the base interface of the walls on both floors, as shown in Fig. 9(a), and (b). The bed joint below the first course of bricks was carefully removed progressively, firstly on the first floor (Fig. 9(c) and (d)). A mould with a height of 70 mm was prepared to cast the new consolidation material. Before applying Mape-Antique I, the area was sprayed with water to prevent excessive absorption of water by the bricks and concrete. This cement-free hydraulic binder, with an 18 MPa compressive strength after 28 days, was selected for its superfluid consistency and a maximum aggregate size of 100 µm to prevent the occurrence of voids (Fig. 9(e)). After repairing the first bed joint on the first floor, a 7-day curing period was considered before proceeding with the second floor (Fig. 9 (f)). No repairs were performed on the observed wall cracks, as introducing new materials and reinforcement could have influenced the structural behaviour.

Besides the repair of the base interface, additional weight, which represented live loads, was placed on both floors. This representative live load was calculated in accordance with European codes EN 1991-1-1 2002 and EN 1990:2002+A1 (2005). The design load combination was taken as $G_k + \psi_2 q_k$, where the quasi-permanent factor for the variable action (ψ_2) was assigned a value of 0.3. The structure was classified as Category A (domestic and residential use), with a uniformly distributed load (q_k) of 2.0 kN/m^2. This resulted in an additional load of 8.4 kN per floor, leading to a total imposed vertical load of 16.8 kN. The weight was applied by filling portable pools with water, and the height of the water was adjusted to achieve the required load (0.11 m), see Fig. 10. Test 1 corresponds to a total weight of 120.5 kN, while Test 2 was imposed with 137.3 kN (Table 5).

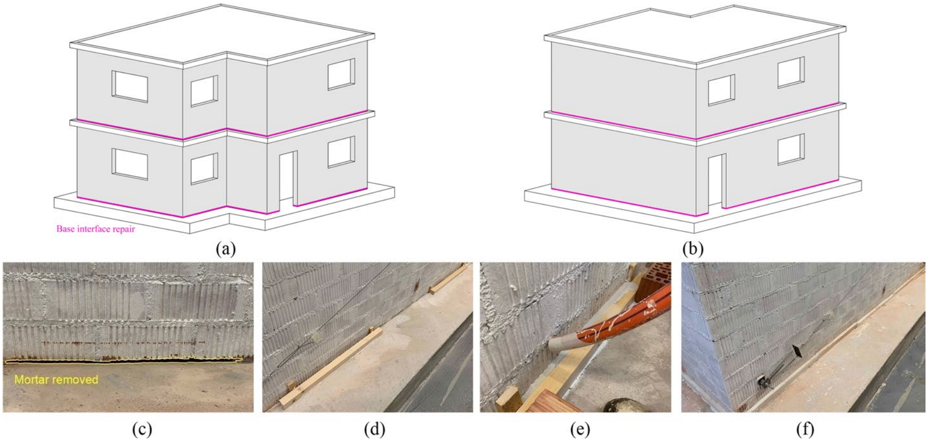

(a) (b)

(c) (d) (e) (f)

Fig. 9 Repair of the base interface along the perimeter (highlighted in pink) to restore the wall-foundation or slab connection after Test 1: (**a**) North-West façade, (**b**) South-East façade, (c) removal of the cement-based mortar, (**d**) preparation of the formwork, (**e**) filling in Mape-Antique I slurry, and (**f**) end of the application

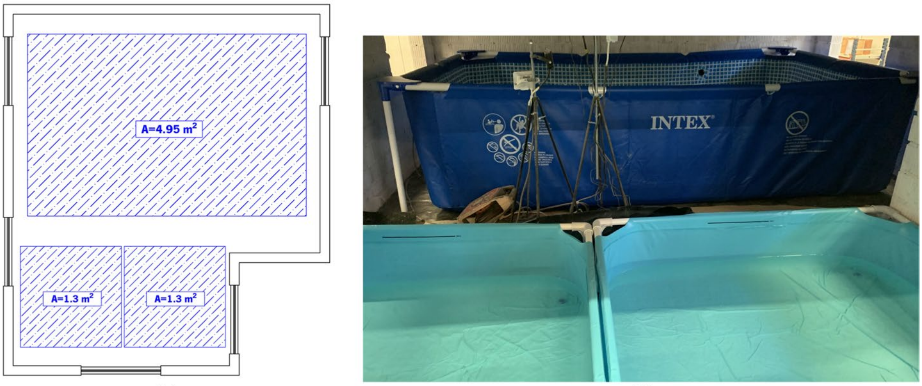

(a) (b)

Fig. 10 Arrangement of the additional weight to replicate live load on each slab: (**a**) visual representation of the water pools and their positioning on the building plan (blue colour indicates the water pools), and (**b**) portable pools filled with water on each floor

Table 5 Summary of the boundary interface conditions and total weight of the structure in Test 1 and Test 2

Test No.	Boundary Interface	Condition	Total Weight
1	M10 mix (Cement-based mortar)	As the built structure	120.5 kN
2	Mape-Antique I (Lime & Eco-pozzolan based)	Repaired boundary + additional weight	137.3 kN

2.4 Material characterisation

This section presents the characterisation of the materials used during construction, namely clay brick units, Grade M10 pre-mixed mortar, concrete, and masonry as a composite material. For this purpose, the experimental campaign includes obtaining the density of the clay brick unit (EN 1015-10 1990), compression test on masonry units (EN 771-1 2000), mortar (EN 1015-11 2007) and concrete (EN 12390-3 2019), and flexural test on mortar (EN 1015-11 2007). For the masonry wallets, the following experimental tests, such as uniaxial compression test (EN 1052-1 1999), flexural strength test (EN 1052-2 1999), initial shear test (EN 1052-3 2002), diagonal compression test (ASTM E 519–02 2002) were carried out. The key mechanical properties of the materials are summarised in Table 6. For further details, the reader is referred to Aşıkoğlu (2024) and Aşıkoğlu et al. (2025).

2.5 Dynamic identification

Six dynamic identification tests were performed in four stages of the quasi-static testing, as listed in Table 7, to (i) identify the modal properties of the built-in structure and define the load pattern (DI0), (ii) quantify the evolution of the damage (DI_T1), and (iv) evaluate the influence of modifications implemented on the building on its dynamic behaviour (DI_RF and DI_WF). The dynamic identification test for obtaining the dynamic properties of the structure in the elastic state (DI 0, as built structure and before testing, see Fig. 8) was used to derive the load pattern representing the first-mode proportional (inversely triangular)

Table 6 Summary of material properties obtained through characterisation tests

Mortar				
Compressive strength of a cube	$f_{c,cube}$	N/mm^2	10	(EN 1015-11 2007)
Compressive strength of a cylinder	$f_{c,cylinder}$	N/mm^2	8	
Young's modulus	E	N/mm^2	3900	
Flexural strength	f_{cfm}	N/mm^2	2.3	
Clay brick				
Density of the brick unit	ρ	kg/m^3	1651	(EN 1015-10 1990)
Compressive strength in direction:				
A: Perpendicular to the bed joint	f_c^A	N/mm^2	15	(EN 771-1 2000)
B: Perpendicular to the head joint	f_c^B	N/mm^2	3.5	
C: parallel to the bed and head joint	f_c^C	N/mm^2	9.6	
Concrete				
Foundation:				(EN 12390-3 2019)
Characteristic compressive strength	$f_{ck,m}$	N/mm^2	15	
Characteristic compressive strength at an age *t**	$f_{ck,m}\,(t)$	N/mm^2	13	
Slab:				
Characteristic compressive strength	f_{ck}	N/mm^2	25	
Characteristic compressive strength at an age *t**	$f_{ck,m}\,(t)$	N/mm^2	21	
Masonry wallets				
Characteristic flexural strength parallel to the bed joint	f_{xk1}	N/mm^2	0.27	(EN 1052-2 1999)
Characteristic flexural strength perpendicular to the bed joint	f_{xk2}	N/mm^2	0.51	
Shear strength (=tensile strength)	$\tau_{max} = f_t$	N/mm^2	0.89	(ASTM E 519–02 2002)
Shear modulus	G	N/mm^2	2550	
Characteristic compressive strength	f_{ck}	N/mm^2	6.6	(EN 1052-1 1999)
Young's modulus	E	N/mm^2	6065	
Characteristic initial shear strength	f_{vok}	N/mm^2	0.26	(EN 1052-3 2002)
Friction coefficient	μ_o	-	0.67	
Internal friction coefficient	α_k	degree	33.8	

* The compressive strength tests for concrete were performed shortly before the quasi-static testing of the building. Unlike code specifications, which require testing at 28 days, the specimens were older at the time of testing. Thus, the characteristic compressive strength at an age t takes the potential ageing effects into account

load application. Dynamic identification No. 2 provides information on the degradation of the dynamic properties at three increasing load levels (DI 45_T1, DI 75_T1 and DI F_T1) by comparing each one with its reference, DI 0, or its previous test. Dynamic identification tests No. 3 and 4 aimed at evaluating the effect of modifications implemented in the damaged structure, namely the repairing (DI RF) and the introduction of additional weight (DI WF). In this case, DI RF was compared with the results at the end of Test 1 (DI F_T1). The repaired model presents the same accumulated damage but has different boundary conditions attributed to the repair at the boundary interface on the first and second floors. DI RF was further compared with the results of the dynamic identification test No. 4, carried out on the repaired building with additional mass (DI WF).

An output-only technique, which relies on ambient vibration testing (AVT), was adopted to determine the dynamic properties of the structure. In total, eight different setups were

Table 7 Summary of the dynamic identification tests performed during different stages of the experiment

Stage	DI Test	Notation	Description
1	As the built structure (Initial condition)	DI 0	Dynamic identification test on the built-in structure, before testing
2	Quas-static testing (Test 1)	DI 45_T1	Dynamic identification test at the end of the cycle with 45% BSC
		DI 75_T1	Dynamic identification test at the end of the cycle with 75% BSC
		DI F_T1	Dynamic identification test at the end of Test 1
3	After repair and before additional weight	DI RF	Dynamic identification test after the boundary interface repair
4	After repair and additional weight (Before Test 2)	DI WF	Dynamic identification test after the introduction of additional weight

implemented, each containing eight uniaxial accelerometers (model PCB 393B12, with a frequency range of 0.15 to 1000 Hz, a sensitivity of 10000 mV/g, and a resolution of 8 μg). Two of the accelerometers were considered as references and kept in the same position for all measurements. The other six accelerometers were relocated according to the relevant setups, as illustrated in Fig. 11. This provides a set of 64 measurements for each dynamic identification (DI), ensuring a detailed identification of the mode shapes at the corners and the middle span of the walls. Considering all the dynamic identification tests presented in Table 7 (from No. 1 to No. 4.), the dataset contains 384 acquisitions. Measurements for each setup were taken for 20 min at a sampling frequency of 200 Hz.

The acquired data were processed through ARTeMIS Modal v.7.0, 2023 using Subspace Stochastic Identification – Unweighted Principal Component (SSI-UPC), as it provided results with higher precision and lower complexity percentages in the present case. The initial AVT, referred to as DI 0, enabled the identification of the first three global vibration modes of the undamaged building, as presented in Fig. 12. The first longitudinal mode registered a natural frequency of 23.9 Hz, while the frequency of the first transverse mode was found to be 25.1 Hz. These two modes were primarily governed by translational motion, though the transversal mode exhibited a slight rotational influence. On the other hand, a predominant torsional mode was detected at a natural frequency of 46.0 Hz, demonstrating pure rotational behaviour. The eigenvectors derived from DI 0 were then used to define the loading protocol and compared with the subsequent phases to evaluate the stiffness degradation.

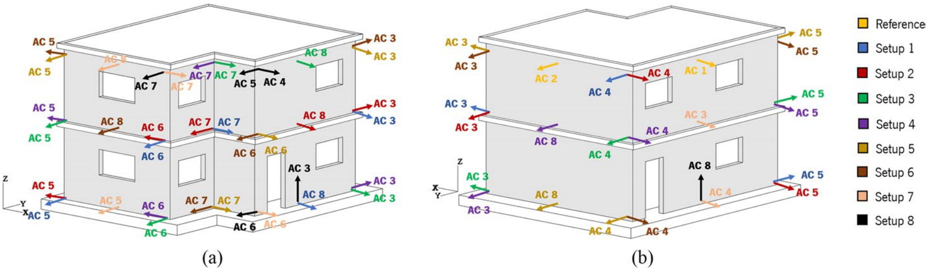

Fig. 11 The layout and sensor directions for the AVT: (**a**) North-West, (**b**) South-East façade

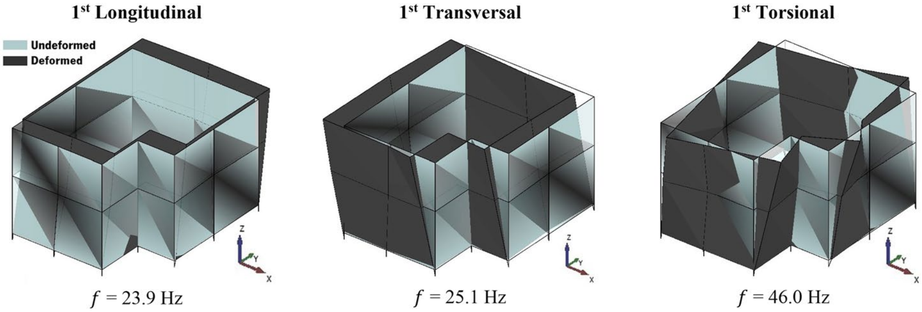

Fig. 12 The first three mode shapes and natural frequencies obtained from the undamaged building, DI 0

2.6 Testing procedure and loading protocol

Cyclic quasi-static tests were conducted along the transverse (X) direction of the experimental building (Fig. 13(e)). This direction was selected based on the modal characteristics identified through dynamic identification and the pronounced influence of eccentricity caused by the setback. The first transverse mode, with a natural frequency of 25.1 Hz, exhibited a rotational influence, indicating a more substantial coupling effect due to plan irregularity. Compared to the longitudinal direction, the transverse eccentricity had a greater impact on the structural response (Fig. 2). Accordingly, the load protocol was defined based on the first transverse mode, leading to a ratio of 1.0:0.6. This meant that during testing, the first floor was subjected to 60% of the load applied on the second floor (Fig. 13(a) and Fig. 13(b)). This ratio was maintained throughout both Test 1 and Test 2. However, translating this idealised loading scheme into a practical testing procedure required accommodating the limitations imposed by the experimental setup and control system. Several constraints influenced the testing procedure, such as:

- The control software lacked synchronised operation of the two actuators. Consequently, the load application was executed manually.
- To mitigate the shortcomings of the manual procedure, the load in each cycle was applied incrementally rather than imposing target values instantaneously. Each actuator followed the same loading protocol with a different magnitude of force, while preserving the constant ratio of 1.0:0.6. Thus, a stepwise loading approach was adopted (Fig. 13(c) and Fig. 13(d)). The load was initially applied to the first floor, in step i. In the next step $i+1$, the load increment was applied on the second floor, while the load increment previously applied on the first floor was held constant (Fig. 13(f)). The load increments were applied gradually, which helped maintain a consistent ratio between the floors without introducing significant variation. This proved to be an efficient compromise while addressing the limitations of the setup.
- The first two cycles during Test 1 were applied using displacement control. The structure was susceptible to even minor displacements, and maintaining the desired target displacements on each floor proved to be challenging. Significant variations in load and displacement resulted in instability in the ratio among the floors.
- To ensure a stable load pattern, force control was implemented. The loads were applied in force control as cycles which alternated between positive and negative directions in two ways for Test 1 (Fig. 13(a)), while the cycles were one-way in Test 2 (Fig. 13(b)).

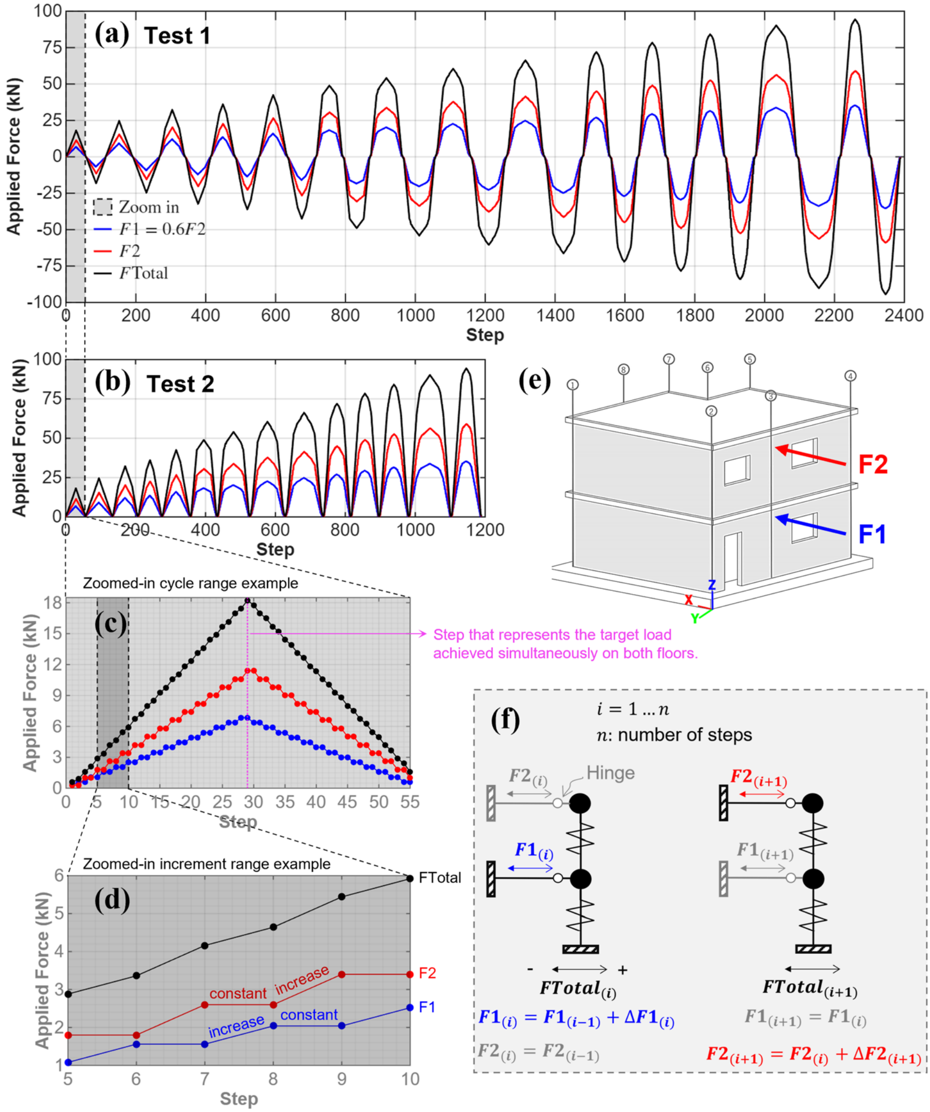

Fig. 13 The testing procedure and load protocol utilised for cyclic force control during Test 1 and Test 2

It should be noted that a predefined velocity rate of 0.002 mm/s, the lowest rate possible, was used during the loading process. The number of steps in each cycle varied mainly to avoid repeating the same increments (particularly in the linear phase) and to reduce the time needed to complete a cycle. The duration and the load steps of each cycle differed. Throughout the testing process, each cycle was treated as an individual application, allowing flexibility to continue tests on different days and at different time frames. The manual load application technique offered control over time, allowing sufficient duration to observe damage at the target force in each cycle, particularly when the maximum crack opening occurred. To this end, the target forces applied on each floor are listed in Table 8. For a detailed stepwise, incremental, and sequential load application, the reader is referred to the dataset available in (Aşıkoğlu et al. 2025).

In Test 2, the loading protocol was modified to apply one-way cyclic loading in the positive transverse direction, as illustrated in Fig. 13(b). This change was based on the insights gained from Test 1, where two-way cyclic loading caused significant detachment of structural components at the base, leading to a notable reduction in boundary stiffness. To avoid repeating this failure mechanism and to ensure a more stable response under force-controlled loading, a one-way cyclic loading approach was adopted. Although the two-way cyclic load protocol on Test 1 more closely represented realistic hysteretic response, the one-way cyclic loading in Test 2 was deemed more appropriate for maintaining structural integrity and is consistent with the assumptions commonly used in numerical simulations, which are typically performed under unidirectional loading.

3 Test results and discussion

This section presents and discusses the key results of the experimental campaign, focusing on the damage analysis, drift response, hysteretic behaviour, the definition of the capacity curve and damage limits, as well as the changes observed in the modal properties.

3.1 Damage analysis and drift response

The evolution of damage, along with the displacement response and inter-story drift profiles at each load step, is analysed to provide a comprehensive understanding of the buildings′ response. A detailed visual inspection of the cracks was conducted during and after the experimental test. Figure 15 shows the evolution of damage throughout the load cycles, where the lateral load was increased by 5% in each cycle, including crack initiation and their subsequent propagation. Red marks indicate damage caused by lateral loading in the positive transverse direction (X), while blue represents the cracks that developed during the loading in the negative transverse direction (-X).

Table 8 Target force applied on the first and second floors in each cycle for Test 1 and Test 2

Cycle	F1 (kN)	F2 (kN)	Total (kN)
3*	6.84	11.40	18.24
4	9.24	15.40	24.64
5	12.12	20.20	32.32
6	13.56	22.60	36.16
7	15.96	26.60	42.56
8	18.36	30.60	48.96
9	20.28	33.80	54.08
10	22.68	37.80	60.48
11	24.84	41.40	66.24
12	27.00	45.00	72.00
13	29.40	49.00	78.40
14	31.56	52.60	84.16
15	33.84	56.40	90.24
16	35.40	59.00	94.40

* Force-control load application starts from Cycle 3

Given that different loads were applied on the first and second floors, the Total Base Shear Coefficient ($TBSC$) accounts for the cumulative applied load from both actuators (F_1 and F_2), divided by the total weight (W_{Total}) of the structure, as given in (Eq. 1). The total weight refers to the entire weight of the building during Test 1, and includes both the self-weight of the structure and the additional weight applied to simulate the live load during Test 2.The Base Shear Coefficient (BSC_2) on the second floor considers only the force applied by the actuator (F_2) located on the second floor, divided by weight, W_2, on the second floor (Eq. 2).

$$TBSC = \frac{F_1 + F_2}{W_{Total}} = \frac{F_1 + F_2}{W_1 + W_2} \tag{1}$$

$$BSC_2 = \frac{F_2}{W_2} \tag{2}$$

The structural response is examined in terms of absolute in-plane displacement ($u_{f,n}$) and inter-story drift ratio ($\delta_{\ int}$) profiles in the transverse (X) direction. The inter-story drift ratio between the two subsequent floors is defined as the ratio of the relative displacement, ($\varDelta\, u_n$), at the control point n to the inter-story height of the floor, h_f, using (Eq. 3). Similarly, the total drift ratio in the transversal direction on the second floor ($\delta_{\ All,av}$), is calculated through the ratio between the average of absolute displacements measured on the second floor, $u_{2,n}$, considering all control points ($n\ =\ 8$ in Test 1), and the total height of the building, H (Eq. 4).

$$\delta_{\ intn} = \frac{\varDelta\, u_n}{h_f} \times\ 100\ = \frac{u_{f,n} - u_{(f-1),n}}{h_f} \times\ 100 \tag{3}$$

$$\delta_{\ All,av} = \frac{\sum{}_1^n u_{2,n}}{n} \times \frac{1}{H} \times 100 \tag{4}$$

Displacement profiles at alignments L1X-L2X, L4X-L5X, and L6X-L7X for South, North1 and North2 walls are shown in Fig. 15, respectively. In-plane behaviour was studied for both positive and negative transversal (X) directions concerning six Total BSC levels, namely 0.30, 0.60, 0.65, 0.70, 0.75, 0.78 (and 0.74 for negative direction). The load steps, identifying the crack initiation until failure, were taken into consideration. A total BSC value of 0.30, within the linear range, was also considered to examine the changes in displacement referring to elastic state and stiffness degradation. Due to the lack of LVDTs at L1.6X and L1.2X locations, it was assumed that the measured deformation at L1.6X and L1.2X would be respectively equal to L1.7X and L1.1X, see Fig. 6.

The damage analysis indicated no visible cracks until the applied lateral load reached 60% of the total weight of the structure (total BSC = 0.60). The average drift ratio on the second floor ($\delta_{\ All,ave}$) was measured at 0.020% (0.62 mm) in the positive direction and 0.028% (0.86 mm) in the negative direction (Fig. 14a). Crack initiation was identified at low drift values recorded on the first floor, with bed joint cracks appearing at the south-west corner at an inter-story drift ratio of 0.012% in the negative direction. see Fig. 15(c). Crack occurrence was primarily driven by the load applied in the negative direction. Signs

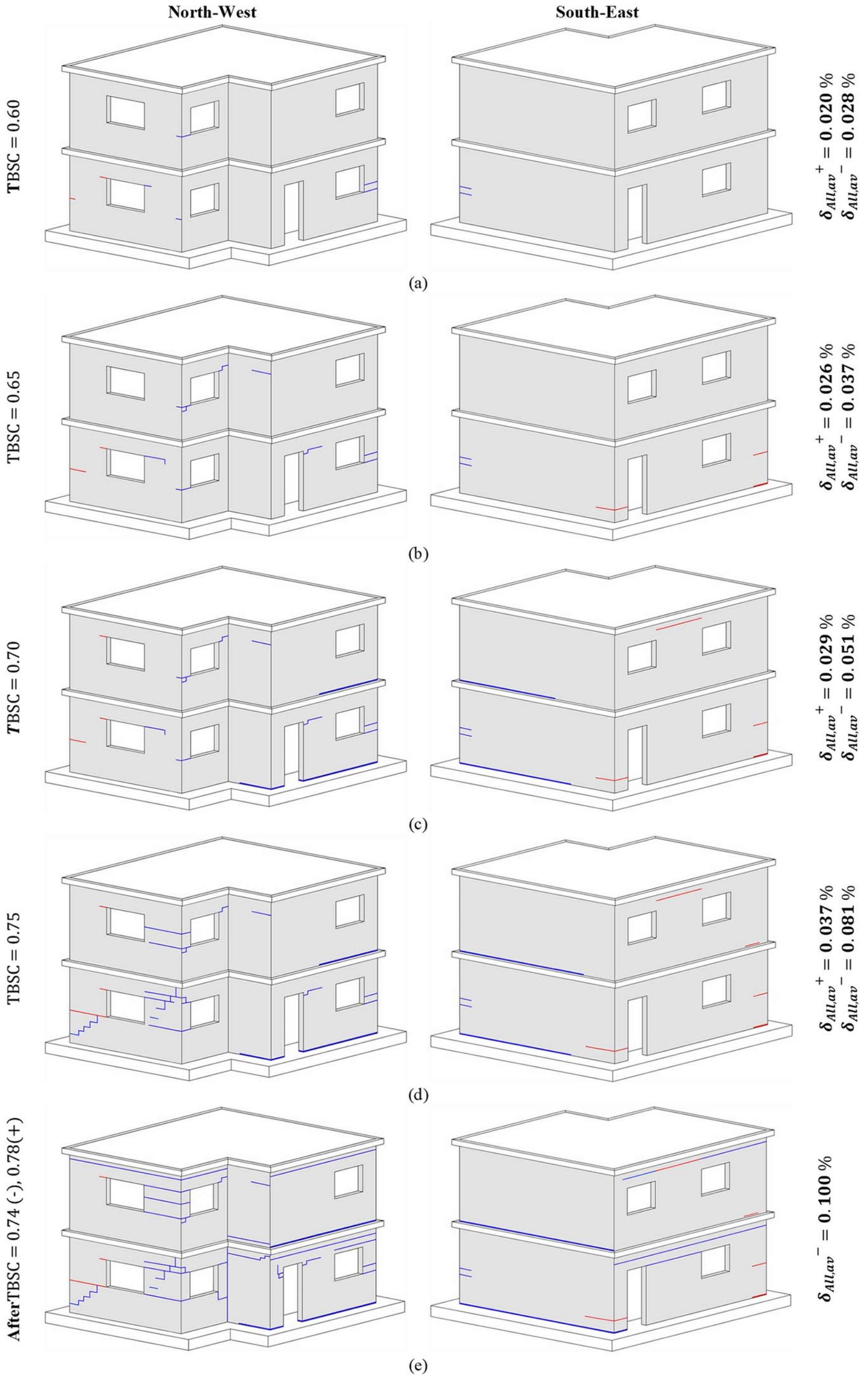

Fig. 14 Evolution of damage throughout Test 1. The red colour refers to damage due to loading in the positive direction while the blue colour indicates cracks as a result of negative loading

of flexural tension cracks were detected on the North1 wall piers on the first floor. Initial cracks align with high-stress concentrations around window and door openings, as well as the corners (specifically, the southwest corner on the first floor and the northwest corner on the second floor). These cracks further expanded to perpendicular walls, highlighting the effectiveness of the flange, as shown in Fig. 17.

Following an increase in the lateral load of 5%, the average absolute drift on the second floor reached 0.026% (0.78 mm), resulting in the extension of flexural tension cracks at the North piers and further propagation to the orthogonal East wall under the loading in the positive direction (see Fig. 14b). The first evidence of uplift occurred at the base of the northeast corner (Total BSC = 0.65 in the positive direction). In the negative direction, the applied lateral load resulted in an average absolute drift of 0.037% (1.11 mm) on the second floor, causing crack occurrences along the mortar and brick interface throughout the structure (Fig. 16). A considerable crack developed on the right side of the door opening on the West wall, which was in the perpendicular direction to the load application. This was a clear indication of the flange effect and the torsional rotation characterising the response of

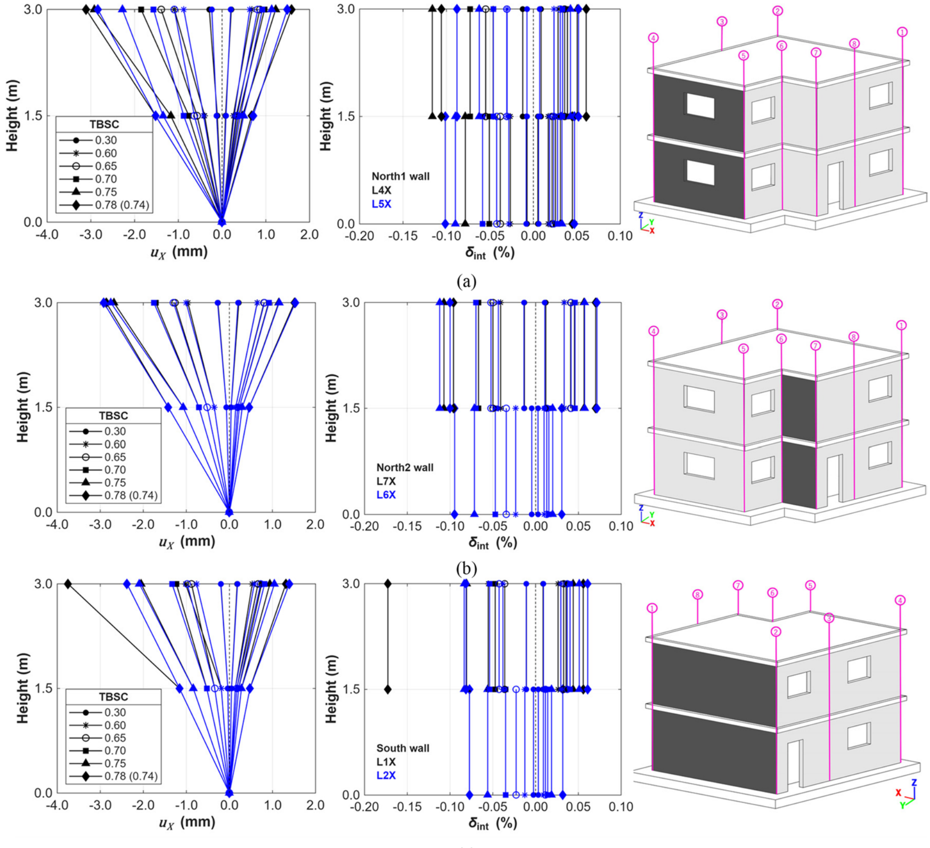

(a)

(b)

(c)

Fig. 15 Displacement and inter-story drift ratio profiles obtained in Test 1 for in-plane walls: (**a**) North1 wall (L4X-L5X); (**b**) North2 wall (L6X-L7X); (**c**) South wall (L1X-L2X)

(a) (b) (c)

Fig. 16 Horizontal cracks observed at the corners: (**a**) northwest corner, (**b**) northeast corner, (**c**) southwest corner

Fig. 17 Absolute biaxial displacements measured on the second floor during Test 1, L2.4 (North1-East corner), L2.5 (North1-West1 corner), and L2.7 (North2-West2 corner)

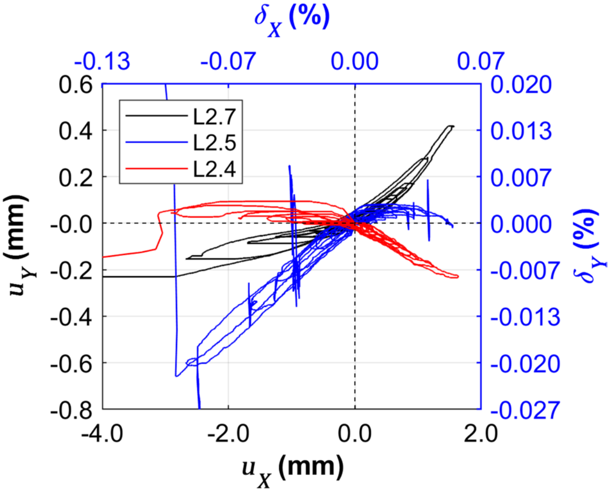

the structure. The second floor developed new cracks that were concentrated on the setback, such as a diagonal crack on the West1 and North2 walls (Fig. 14b).

This aligns with the absolute biaxial displacements measured on the second floor, as shown in Fig. 17. Translational displacements were observed in both u_X and u_Y directions, regardless of the loading orientation. Notably, biaxial displacements were recorded from the early stages of the linear response. The North1-East corner (L2.4Y) was displaced in the negative direction, while the other two corners, the North1-West1 corner (L2.5Y) and North1-East corner (L2.7Y), moved in the opposite direction (Fig. 17). The two corners of the North1 wall, namely L2.4Y and L2.5Y, moved in opposite directions. On the other hand, L2.5Y (North1-West1 corner) and L2.7Y (North2-West2 corner), which were the corners of the setback, were deformed in the same direction. This behaviour indicates the evidence of building rotation, which in turn may explain the occurrences of horizontal and diagonal cracks on the out-of-plane walls.

At a Total BSC of 0.70, crack progression under positive loading cycles was gradual compared to the negative cycles. Horizontal cracks formed primarily along bed joints, with one developing directly beneath the actuator on the second floor and another at the northeast corner (Fig. 14c). A critical shift in structural behaviour was observed at a total drift of 0.051% in the negative direction ($\mathrm{u}_{2,2}=1.52\,\mathrm{mm}$), when the southwest corner began exhibiting prominent rocking behaviour, accompanied by uplifting on both floors (Fig. 18). Among the three LVDTs, only UP2 captured the uplift displacement (Fig. 19a).

Figure 19(a) illustrates that no significant vertical displacements occurred at the base of the North1 wall (UP1 and UP3). Although direct measurements were unavailable at the base of the South façade, UP2, the nearest LVDT, provides insight into the uplift response, capturing vertical displacement at the West2 wall. This behaviour suggests that the South wall likely experienced the most significant vertical displacement, as it was positioned farther from the setback than UP2. The correlation of the uplift displacement (U_{UP}) and the average of all displacements in the transverse direction on the second floor ($u_{2,ave}$) enables the analysis of the onset and progression of the rocking behaviour of the structure. Figure 19(b) illustrates that once the total drift ($\delta_{All,ave}$) exceeded 0.051%, uplift initiated in a nonlinear manner as the lateral load increased, suggesting a transition to rigid body rocking motion.

At the Total BSC of 0.75, total drift ratios of 0.037% (1.10 mm) and 0.080% (2.41 mm) were obtained in the positive and negative directions, respectively. The applied load in the positive direction mainly resulted in the extension of the previous cracks, as illustrated in Fig. 14 (d). In contrast, the applied load in the negative direction caused a diagonal shear crack on the North1 wall (Fig. 20a), with a crack opening of 0.70 mm before the system


(a) (b)

Fig. 18 Uplift deformations observed at the boundary of the: (**a**) Southwest corner on the first floor, (**b**) South wall on the second floor

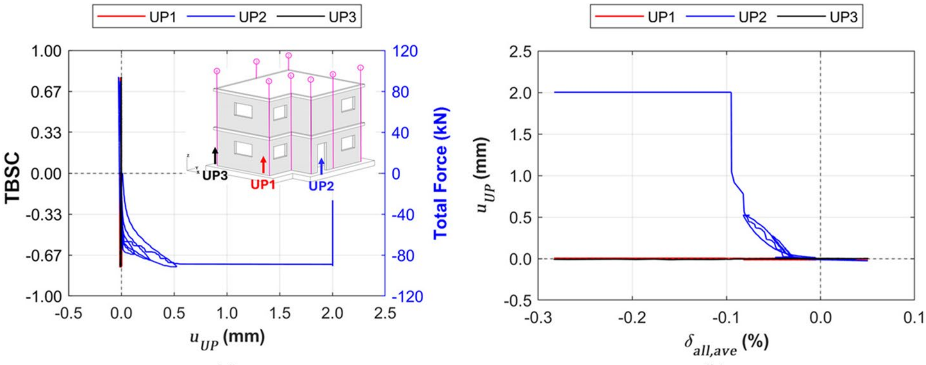

(a) (b)

Fig. 19 Uplift deformations measured at UP1, UP2, and UP3 throughout Test 1 concerning: (**a**) $\boldsymbol{TBSC}$, (**b**) $\boldsymbol{\delta_{All,av}}$

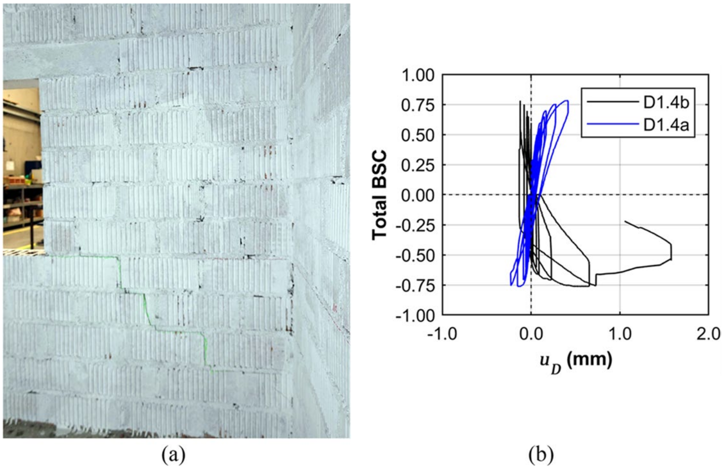

Fig. 20 Diagonal shear crack on North1 wall: (**a**) green line, interior view, (**b**) diagonal crack opening by D1.4a and D1.4b

failed, see Fig. 20 (b). It is interesting to note that, in the case of North 1 wall, flexural cracks initiated on the left-hand pier at an inter-story drift ratio of 0.018%. In comparison, similar flexural cracks appeared on the right-hand pier under the same load applied in the negative direction, associated with a higher inter-story drift ratio of 0.028%. Up to a Total BSC of 0.75, the North1 wall's response was governed by flexure. Still, at this load level, the inter-story drift ratio on the first floor reached an average of 0.084% (based on L1.4X and L1.5X), and the wall developed a diagonal crack, exhibiting a combined flexural and diagonal shear mechanism. Notably, this drift value is significantly lower than those suggested for in-plane walls in the literature (EN 1998-1:2004, 2004; Morandi et al. 2018).

As the final load step progressed to a maximum total drift of 0.049% (Total BSC = 0.78) in the positive direction, the width of the existing cracks increased further, but there was no evidence of new occurrences. Additionally, the load application did not reach its target load in the negative direction, and the structure failed once the Total BSC reached 0.74, which was lower than in the previous cycle. This, indeed, shows that the maximum capacity of the structure was reached in the negative direction. Since the loading procedure was under force control, the experimental system could not maintain the force, and the displacement increased rapidly, resulting in the formation of new horizontal and diagonal cracks. The structural walls were severely detached from their boundary constraints on both floors, as demonstrated in Fig. 14 (e). Consequently, it was decided to stop the test.

Overall, the structural response was characterised by a combined mechanism of flexural deformation and diagonal shear, with the predominant rocking behaviour of the entire structure. The maximum measured longitudinal displacement (u_Y) was observed at L2.5Y. This could explain the occurrence of horizontal and diagonal shear cracks observed on West1 and West2 walls, respectively (see Figs. 15 and 17). With the sudden release of force at the rocking failure point, the structure slid nearly 10 mm and 20 mm from the base of the South and West2 walls, respectively (Fig. 21). The base of the South and West walls was utterly detached from the foundation and displayed significant deformations. However, it was concluded that the structure slid partially due to the deformation measured by LVDT

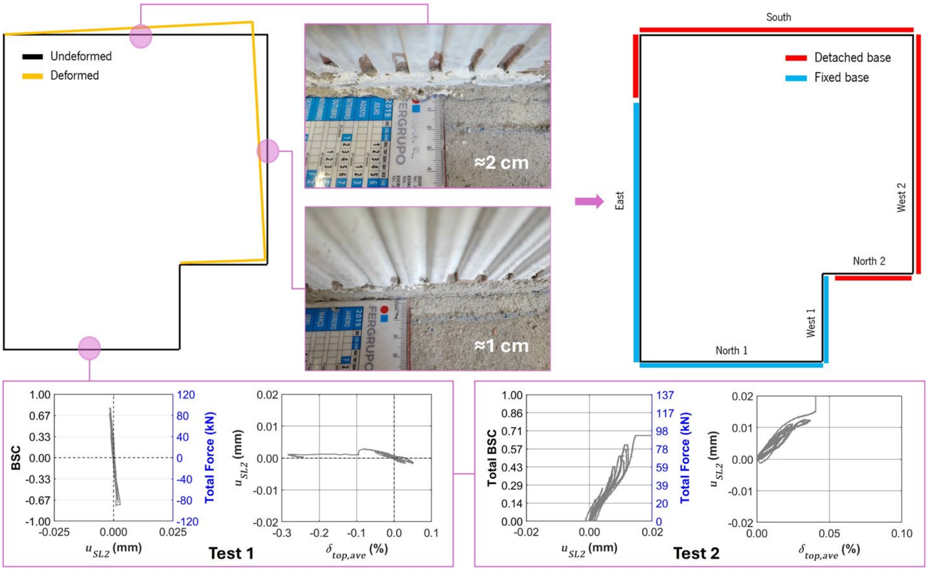

Fig. 21 Visual representation and measurements of residual sliding displacement at the base of the structure after Test 1. Additionally, sliding displacements recorded during Test 2 are presented at their respective locations

SL2, which was significantly less than 0.01 mm, indicating no significant sliding below the North1 wall. A summary of inter-story drift ratios, total drift ratios, and their associated damage mechanisms is presented in Table 9 for each in-plane wall at various levels of Total BSC.

Figure 22 presents the progression of damage (indicated in blue) observed during Test 2, after boundary repair of the structure and more weight was added. Notably, no damage was recorded at the base of the structural walls, similar to uplift, highlighting the efficiency of the boundary interface repair conducted after Test 1. The observed damage, on the other hand, was predominantly linked to the activation of pre-existing cracks, which were observed to open and close during the test. Onset diagonal shear crack formed on the North1 wall, while horizontal cracks were observed at the base of West1 wall and the East wall on the second floor. It is stressed that the horizontal cracks transitioned directly above the first brick course rather than the repaired mortar layer, which suggests the efficiency of the repairing method. This implies that the repaired boundary interface contributed to the redistribution of the strains, thereby preventing damage along the boundary interfaces. This finding is consistent with the displacement measured on the South wall, which was relatively lower compared to other in-plane walls, as presented in Fig. 24. The maximum displacement recorded on the South wall was 1.0 mm, with less than 0.05 mm observed on the first and second floors, respectively.

Figure 23 presents the results of the displacements and inter-storey drifts of the building obtained in Test 2, focusing on the overall performance. The maximum displacement measured on the North1 wall (by LVDT L2.4X) was nearly 1.6 mm, which corresponds to a 0.05% total drift on the second floor. The absolute in-plane displacement on the North2

Table 9 Summary of the damage progression throughout Test 1

TBSC	Wall	Floor	δ_{int}(%)	Damage Mechanism	$\delta_{All,av}$(%)
0.60	South	1	0.012 (-)	Bed joint cracks at West2-South corner	0.020 (+) 0.028 (-)
	North1	1	0.018 (+)	Initiation of flexural cracks on the left-hand pier	
	North1	1	0.028 (-)	Initiation of flexural cracks on the right-hand pier	
0.65	North2	2	0.052 (-)	Flexural crack on the top right	0.026 (+) 0.037 (-)
	South	1	0.011 (+)	Horizontal cracks at the southeast corner	
	North1	1	0.022 (+)	Uplift at the base of the North1-East corner	
	West1	2	N.A.	Development of a diagonal shear crack	
	West2	1	N.A.	Occurrence of horizontal cracks	
0.70	South	1	0.035 (-)	Uplift deformations, rocking behaviour, and the occurrence of a horizontal crack at the southeast corner	0.029 (+) 0.051 (-)
	South	2	0.047 (-)	Uplift deformations, rocking behaviour	
0.75	South	1	0.056 (+)	Extended horizontal crack, Rocking	0.037 (+) 0.081 (-)
	North1	1	0.083 (-)	Development of a diagonal shear crack	
	North1	1	0.032 (+)	Flexural failure of the left-hand pier	
	North1	2	0.062 (-)	Flexural failure of the right-hand pier	
0.74 (F)	South	1	0.077 (-)	Detached along the mortar interface at the boundary conditions, shear sliding	0.100 (-)
	South	2	0.170 (-)	Detached along the mortar interface at the boundary conditions	

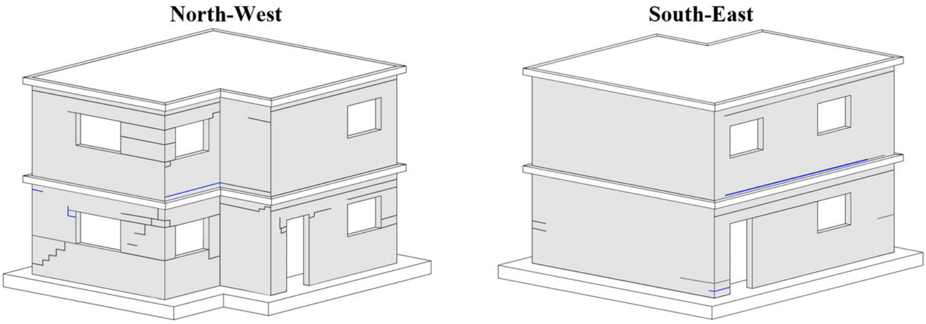

Fig. 22 Evolution of damage at the end of Test 2

wall was measured as 0.5 mm on the first floor, while the second floor reached up to 1.5 mm. Consequently, an inter-story drift ratio of almost 0.07% was obtained on the second floor, with half of this amount on the first floor. Inter-story drift ratio profiles illustrate that the stress concentration and potential damage were distributed between the first and second floors.

Biaxial displacements depicted a similar trend during Test 2, as presented in Fig. 24. Displacements of approximately 0.4 mm were measured at L2.4Y and L2.7Y. Yet again, L2.4Y responded in the negative direction while L2.7Y (North2- West2 corner of the setback) moved in the positive direction, indicating the plan rotating counterclockwise. Nevertheless, L2.5Y exhibited displacements of less than 0.1 mm during Test 2, suggesting that this corner likely remained stationary. It is important to note that the response observed in Test

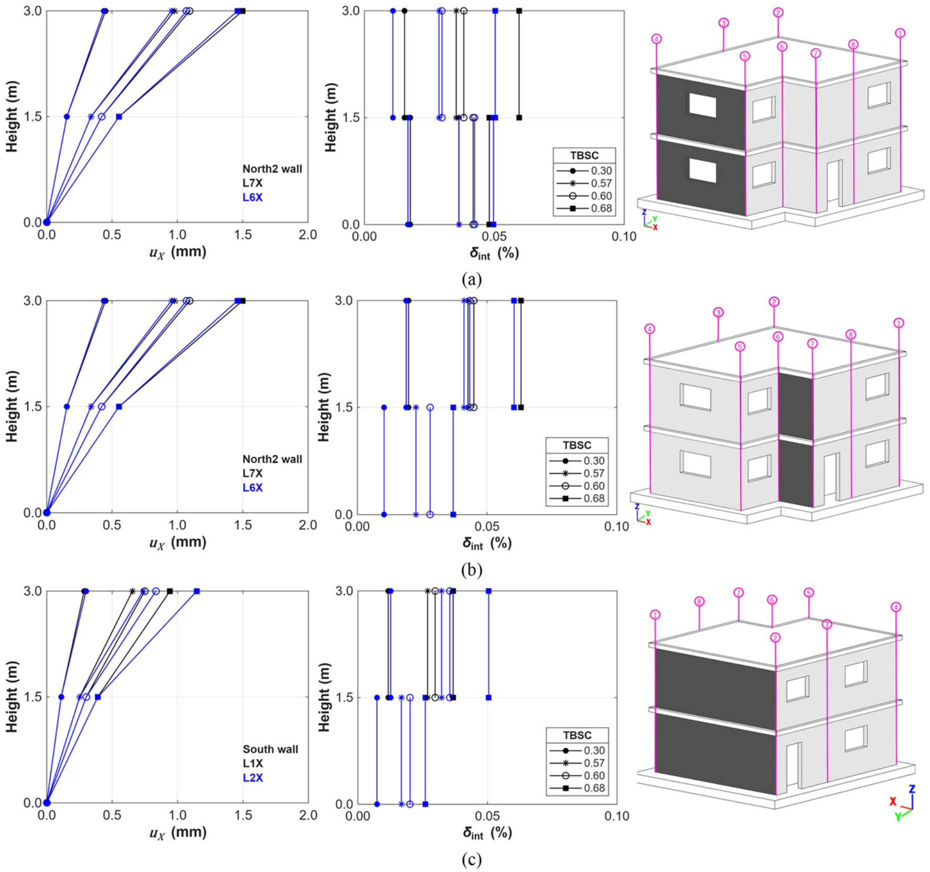

(a)

(b)

(c)

Fig. 23 Displacement and inter-story drift ratio profiles obtained in Test 2 for in-plane walls: (**a**) North1 wall (L4X-L5X); (**b**) North2 wall (L6X-L7X); (**c**) South wall (L1X-L2X)

Fig. 24 Absolute biaxial displacements at L2.4 (North1-East corner), L2.5 (North1-West1 corner), and L2.7 (North2-West2 corner) during Test 2

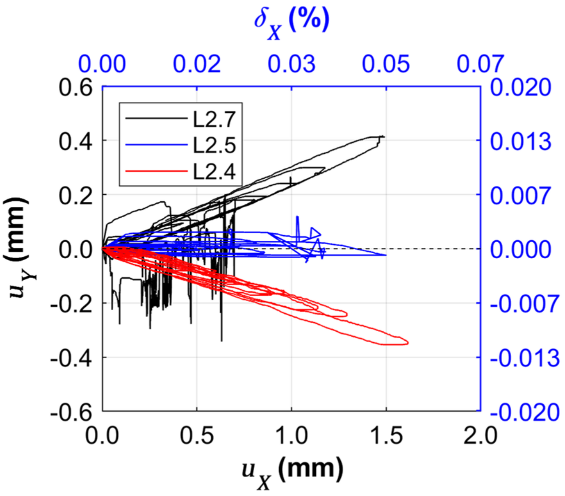

2 was limited to one-way cyclic load application. In contrast, a two-way cyclic load induces damage that can contribute to deformations in the opposite direction.

3.2 Hysteretic behaviour

The hysteretic behaviour was examined to understand the extent of energy dissipation and inelastic behaviour. The relative displacements at each floor (?u) and the base shear coefficient corresponding to each floor was evaluated according to Eq. 1 and Eq. 2, and considered to construct the hysteresis diagrams for each in-plane wall. Figure 25 presents hysteresis diagrams representing the lateral response on each in- plane wall on the first and second floors, namely North1 (L4X-L5X), North2 (L6X-L7X), and South walls (L1X-L2X).

In general, the hysteretic response of the building during Test 1 indicated that energy dissipation was initiated, but stiffness and strength degradation were relatively minimal, see Fig. 25. Despite the visible cracks and deformations, the building remained in the pre-peak regime. It was not possible to capture the post-peak behaviour of the structure. Therefore, these plots do not provide sufficient information to assess the ductility of the structure. Concerning the lateral load capacity, the structure remained mainly within the pre-peak phase under the positive load direction, making it difficult to determine its state in terms of lateral strength.

Although the post-peak response was not possible to capture entirely, the maximum $TBSC$ in the negative direction was found as 0.75, with a maximum inter-story drift value of 0.11% on the first floor. On the other hand, the BSC_2 reached 0.98 at the peak lateral load on the second floor. An abrupt change in force and displacement was observed beyond these two points, corresponding to the end of the test. As previously stated, the building's response was primarily governed by rocking behaviour, which explains the minimal stiffness degradation observed. After the structure experienced rocking and the wall boundary interfaces detached, additional sliding occurred. The force-controlled system was unable

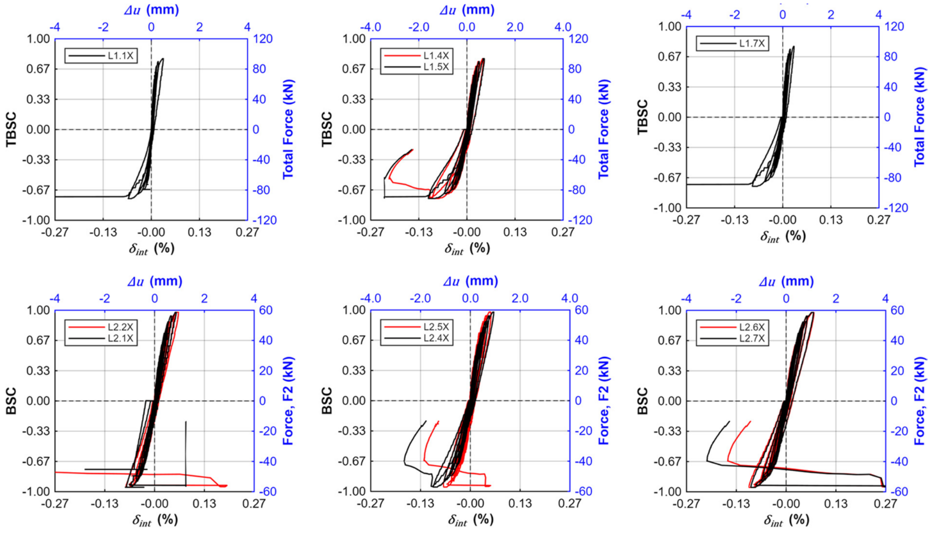

Fig. 25 Hysteretic response of the in-plane walls throughout Test 1 (Note that the axis limits may vary)

to sustain the applied load, resulting in the sudden, higher deformation observed in the diagrams.

The hysteresis diagrams obtained from Test 2 are shown in Fig. 26. The maximum $TBSC$ achieved was 0.68 on the first floor, while the highest relative BSC_2 reached 0.85 on the second floor. These values are lower than those obtained from Test 1, given that increased total weight was considered (Fig. 26). Expanding cyclic loops indicate that the energy dissipation increased with every load increment. On the other hand, the South and North1 walls on the second floor displayed non-uniform displacement along their length, indicating the influence of torsion. This behaviour was less apparent on the first floor, suggesting that torsional effects were more pronounced on the second floor.

3.3 Definition of capacity curve and damage limits

The performance level of a structure is represented through the deformation level defined as performance limit states, such as Fully Operational, Operational, Life Safety, and Near Collapse (EN 1998-1:2004, 2004). However, establishing these performance limit states is a challenging task and might require evaluation of deformations at the local, global, or both levels (Lagomarsino and Cattari 2015; Graziotti et al. 2017; Vanin et al. 2017; Kallioras et al. 2018, 2020; Morandi et al. 2018; Korswagen 2024). The performance limits derived from individual in-plane walls, as given in the codes, are commonly used. However, their applicability at the structural level, where multiple components interact, remains uncertain. Since the capacity curves of structures with box-behaviour are defined by considering the global behaviour, the limits based on individual components may not directly correspond to the overall response.

A limited number of studies defined performance limits through shake-table tests (Graziotti et al. 2017; Kallioras et al. 2018) or cyclic quasi-static tests (Esposito et al. 2019). Shake-table tests, in fact, often fail to capture the post-peak response without resulting in

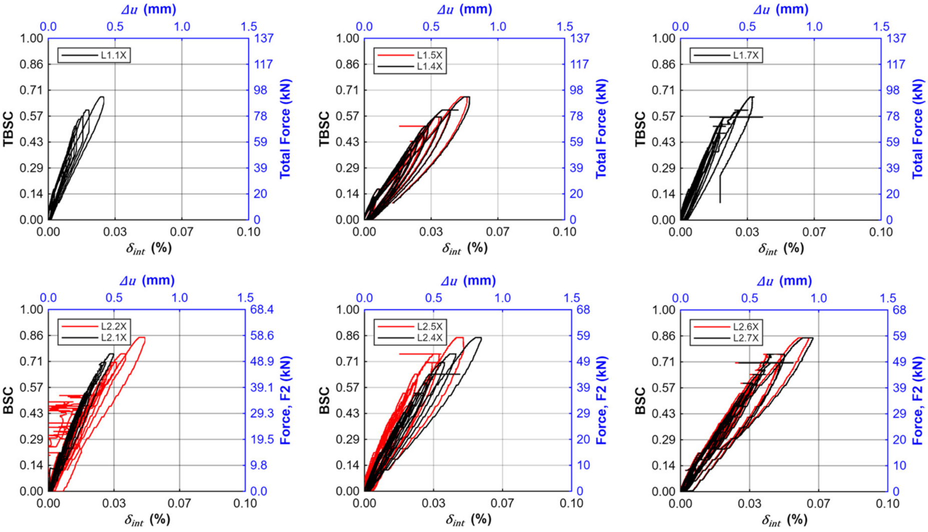

Fig. 26 Hysteretic response of the in-plane walls throughout Test 2: (**a**) South Wall, (**b**) North1 Wall, (**c**) North2 Wall

imminent collapse (Lourenço et al. 2013; Magenes et al. 2014; Avila et al. 2018). As a result, the capacity curves derived from these tests provide limited information on the nonlinear response between the maximum lateral strength and collapse. Incremental quasi-static loading shows a potential to address this research gap. To date, the performance limit definition through quasi-static testing has focused on the structural element level (Vanin et al. 2017; Morandi et al. 2018; Korswagen 2024). Notably, Esposito et al. (2019) stand out as the only one to propose performance limits based on the global structural response through quasi-static testing. Drift limits provided in codes may be feasible to consider for individual components, such as piers. However, the observed response indicates that damage may initiate at drift levels lower than those prescribed by codes. This suggests that such limits may be unconservative when applied at the building scale. Nevertheless, the structure's ability to redistribute internal forces contributes to delaying global failure despite early local damage. This highlights the importance of considering system-level behaviour, including force redistribution and component interaction, as these mechanisms play a critical role in enhancing overall structural resilience.

3.3.1 Control node selection and capacity curve

The capacity curve is derived based on a selected control point, typically located on the top floor of the building, which in this case corresponds to the second floor. This implies that the determination of the capacity curve is inherently dependent on the choice of control points if the floor displacements are not uniform. Therefore, the selection of the control point may have some implications on the definition of the capacity curve of an irregular structure, despite having a rigid diaphragm. This aspect must be taken into account, particularly when the irregularity results in torsional behaviour (Avila et al. 2018). For this reason, it was decided to study multiple control points at the level of the slab of the second floor, such as the points with maximum and minimum displacements, the average of all measured transversal displacements, and the average of two displacements located at the centre of mass on the second floor (L2.3X and L2.8X). This allowed for a better understanding of how the control point selection influenced the capacity curve derived in the case of the torsion of the building, which results from plan irregularity in the distribution of the in-plane walls. Figure 27 illustrates the experimental capacity curves obtained for the load applied in the positive and negative directions. These monotonic envelope curves were derived as a function of the total BSC and total drift ratio on the second floor.

The maximum displacement at each cycle, indicating lower stiffness, was measured at L2.4X (North1 wall) while the minimum displacements (indicative of higher stiffness) were recorded by L2.3X (CM). These control nodes were designated as upper and lower bound limits to have an idea of the range of displacements that occurred under the given loading, respectively. Figure 27 shows the difference between the maximum (δ_{Max}) and minimum drift ratio (δ_{Min}) values and their difference increased up to nearly 10% and 30% in the positive and negative direction, respectively. This variation was evident even in the early elastic phase of the structure, emphasising the influence of torsional response attributed to plan irregularity. For instance, the variation was less than 5% until the point at which BSC was equal to 0.6, representing the lateral strength needed for the elastic limit in the positive direction. On the other hand, the difference in the drift ratio at the elastic limit was almost 3 times more in the negative direction.

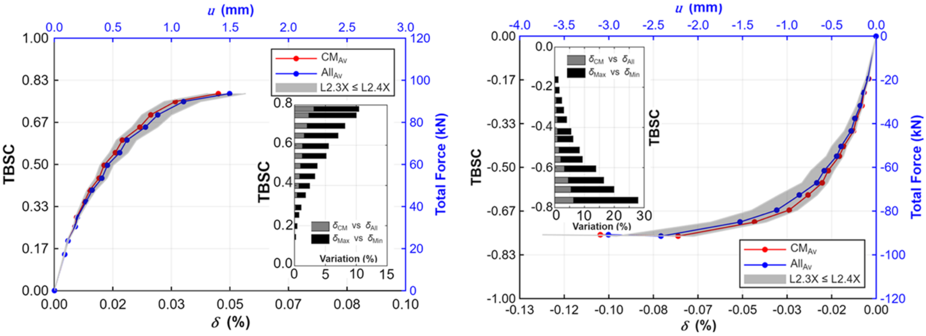

(a) (b)

Fig. 27 Lateral strength and deformation capacity obtained from Test 1, considering different control points and their variation: (**a**) positive direction, (**b**) negative direction

The difference becomes more evident when considering the impact of plan irregularity combined with damage progression. This critical aspect warrants an in-depth discussion. Opting for the control point with maximum deformation is a conservative approach. By selecting the maximum as the control point, the analysis encompasses the scenario in which the structure undergoes the maximum deformation, providing a reliable estimation of unfavourable cases. Conversely, choosing the control point with minimum deformation is deemed conservative. It potentially underestimates the global response in terms of ductility, while overestimating the global stiffness.

This dispersion prompted an interest in comparing the average absolute displacement of CM, $\delta_{CM,av}$, and the average absolute displacement measured at eight lateral LVDTs ($\delta_{All,av}$). In practice, the control point is often referred to as CM to define the capacity curve for cases with a rigid diaphragm. Nevertheless, the question arises regarding the extent to which CM accurately represents the global response, especially when torsional influences are involved. Accordingly, the capacity curve obtained for $\delta_{CM,av}$ and $\delta_{All,av}$ revealed minimal differences. The maximum variation between the two drift ratios was less than 5% under positive loading and nearly 6% under negative loading (Fig. 27). Yet, $\delta_{CM,av}$ was closer to the lower bound limit (lower displacement), indicating a conservative tendency. Ultimately, the capacity curve was established by considering $\delta_{All,av}$ as the overall representative of the response acquired in Test 1. This choice aimed to compensate for the variations among the control points by adopting an averaging approach and taking into account the torsion of the building. The results shown in Fig. 27 give a clear indication of the importance of control node selection to plot capacity curves and, consequently, the compromise to be assumed in the implementation of a performance-based approach. For instance, if the control node with a maximum displacement is considered to derive the capacity curve, the overall deformation capacity of the structure might be overestimated. This is particularly important for the definition of damage limits. Otherwise, selecting a control node with a minimum displacement would lead to an overestimation of the stiffness of the structure.

The same approach was carried out to derive the capacity curve of the building tested after repair (Test 2). The envelopes of the maximum and minimum deformation observed on the second floor (L2.1X and L2.4X), an average of 8 LVDTs, and the average of L2.3X and L2.8X, representing the CM of the second floor, are considered for the discussion. The difference between the maximum and minimum ranges up to 23%, depending on the applied lateral load. Likewise, in Test 1, it is suggested to consider the average of 8 LVDTs, which measured absolute displacements on the second floor, as it is almost the same as the CM. Briefly, the envelopes obtained from Test 1 and Test 2 are compared in Fig. 28 for the positive direction. It is noted that the last point of the curves does not represent the peak lateral load capacity due to the premature end of the tests, particularly in Test 2. Hence, the discussion of the capacity curves was carried out focusing on the pre-peak behaviour. A considerable reduction in initial stiffness was observed in Test 2 compared to Test 1, which could be attributed to the pre-existing damage on the walls. Although a direct comparison between the two tests is not entirely feasible, the energy dissipation observed in Test 2 was significantly lower than in Test 1. This difference could be attributed to the difference in loading conditions between the two tests. Test 1 involved two-way cyclic loading, which contributes to plastic deformations and generally promotes higher energy dissipation. In contrast, Test 2 applied one-way cyclic load, resulting in lower energy dissipation as the structure was subjected to forces only in the positive direction, limiting the extent of hysteretic behaviour and energy absorption.

3.3.2 Damage limits

Despite being unable to reach the post-peak capacity, an attempt to define the damage limits was made for Test 1, assuming that the maximum capacity of the building was reached. The definition of the damage limits was carried out qualitatively, relying on the damage analysis outlined in Fig. 14; Table 9. The damage state classification adopted in this study is aligned with the EMS-98 scale (Grünthal 1998), as it is based on qualitative indicators such as crack distribution, structural integrity, repairability, and user comfort. Accordingly, DL1 (Elastic Limit) marks the onset of cracking, and DL2 (Damage Limitation) may correspond to the peak lateral strength. DL3 (Severe Damage) represents moderate damage accumulation with widespread cracking and localised weakening. DL4 (Near Collapse) represents extensive structural damage, significant degradation in strength, and potential instability.

Figure 29 depicts the damage limits highlighted on the capacity curves in both positive and negative directions. Accordingly, the structural response in the positive and negative transversal (X) direction showed differences, with the building exhibiting more displace-

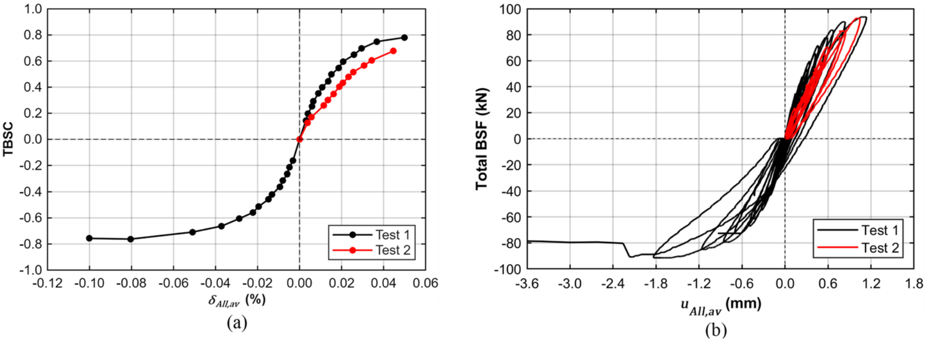

Fig. 28 Comparison of the response in the positive direction from Test 1 and Test 2: (**a**) envelope curves, (**b**) hysteresis curves

ment and a higher progression of damage in the negative direction. This led to slightly different damage limits for each direction. When considering the applied load in the positive direction, two damage limits were estimated, namely δ_{DL1} and δ_{DL2}. The visible crack initiation, corresponding to DL1, was observed at a 0.021% top drift ($\delta_{All,av}$) for 0.60 Total BSC. This drift ratio was identified as δ_{DL1}. The last load step in the positive direction did not indicate signs of significant damage progression because the incremental load was not applied further. Thus, the identification of this point as pre-peak or peak was not feasible since the progression of the damage mechanism after this point was uncertain, but it might indicate the starting point of a plateau. Therefore, it was decided that DL2 in Fig. 29(a) would indicate a potential damage limit and was represented by a dashed yellow line.

When the load is applied in the negative direction, it is safe to assume that the capacity of the building has reached its plateau, as seen in Fig. 29(b). In this case, the damage limit states (DL1 to DL3) were defined as lateral drifts δ_{DL1}, δ_{DL2}, and δ_{DL3} equal to 0.028%, 0.051%, and 0.100%, respectively. The onset of cracks was indicated at a relatively higher δ_{DL1} in the negative direction. The damage limit state DL2 was identified as the drift ratio limit at a point at which the damage mechanism was changed from shear failure to rocking of the entire building. Therefore, δ_{DL2} represented the limit right before the uplift. The lateral drift corresponding to DL3, δ_{DL3}, was defined at 0.100%, because this level of deformation led to a complete loss of adherence at the base of the building. It appears to be reasonable to classify the 0.100% top drift ratio as δ_{DL3} rather than δ_{DL4}, as DL4 mostly signifies structural collapse. As already mentioned, after Test 1, it was possible to repair the boundary interfaces on both floors. At this very last point, the walls did not suffer severe damage (absence of masonry crushing and loss of material) or total collapse to mark it as DL4. In addition, from Test 2, carried out on the repaired building, it is observed that resistance was partially recovered in the positive direction.

3.4 Changes in modal properties

Table 10 presents the changes in natural frequencies due to damage during testing and after repair of the building. The reduction in the percentage of the first transversal frequency compared to the reference was higher than the longitudinal one. This was expected as the

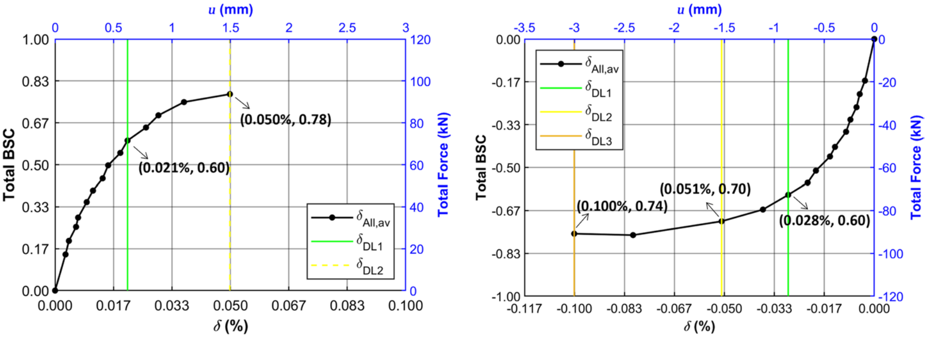

(a) (b)

Fig. 29 Capacity curves obtained from Test 1 and performance limits for the: (**a**) positive direction, (**b**) negative direction lateral loading was applied in the transversal direction, inducing primarily in-plane damage on walls, but also a combined flexural-shear-rocking mechanism of the building. At the end of the cycle with total BSC 0.45 (DI 45_T1), the change in frequencies was minor, with a maximum of 6%, aligning with the expectations, as no visible damage was identified at this stage. The equivalence of the natural frequency values for the longitudinal and transversal modes could be a consequence of the coupling of the modes, once the damage reduces the frequency of the transversal mode. Possibly, processing the acquisition in X and Y separately could provide a better estimation of the first natural frequency, which could be overestimated here. DI 75_T1 (Total BSC = 0.75), instead, indicate a significant damage development, as the frequency values substantially dropped. At the end of Test 1 (DI F_T1), the frequency of the first longitudinal mode was reduced by 23% while the reduction for the first transverse and torsional modes was 25% and 23%, respectively. The natural frequencies of the damaged building were determined to be 18.4 Hz, 18.8 Hz, and 35.2 Hz for the 1st longitudinal, transversal, and torsional mode shapes at the end of Test 1, respectively.

Furthermore, the frequencies obtained before and after the repair at the boundary interface (DI F_T1 vs. DI RF) were compared to determine the extent of its influence on the overall stiffness. The repair increased the frequencies obtained after the damage to the building by 10% in the longitudinal direction, 14% in the transverse direction, and 11% in torsion, confirming the effectiveness of the boundary repair. Nevertheless, complete recovery of the initial frequency was never possible due to the presence of cracks on the masonry walls. Assuming that the repair restored the boundary conditions, a 13% difference in frequency between the DI RF (21.9 Hz) and DI 0 (25.1 Hz) first transversal mode could be attributed to damage to the masonry walls. The comparison between DI RF and DI WF showed negligible differences in frequency (less than 0.5%), despite the added weight being 14% of the structural self-weight. Although the added mass would reduce the natural frequency, it may simultaneously increase frictional stresses at cracked interfaces, thereby increasing the effective stiffness. Therefore, the opposing parameters offset each other, resulting in minimal change observed in the frequency.

After characterising the dynamic properties of the experimental building in different phases, changes in the shape of the modes were studied through the Modal Assurance Criterion (MAC) to investigate the evolution of damage and the effectiveness of modifications. The MAC values were calculated based on the methodology proposed by Ewins (2000), comparing the mode shapes at each dynamic identification with the ones obtained in the undamaged stage, DI 0, see Table 11. The obtained vibration modes exhibited similarities to those illustrated in Fig. 11, as confirmed by the high MAC values. For DI 0 – DI 45_T1, the MAC was 0.96, 0.91, and 0.91 for the first longitudinal, transversal, and torsional modes, respectively. The MAC value of 0.91 in the first transverse direction was lower than the subsequent test (DI 0 – DI 75_T1), likely due to the mode coupling between the first and

Table 10 Frequencies of the first three vibration modes at different stages, with relative changes compared to DI 0 shown in parentheses

DI	1st Longitudinal	1st Transverse	1st Torsional
	f (Hz)	*f* (Hz)	*f* (Hz)
DI 0	23.9	25.1	46.0
DI 45_T1	24.8 (-4%)	24.8 (1%)	43.2 (6%)
DI 75_T1	22.3 (7%)	21.7 (14%)	41.3 (10%)
DI F_T1	18.4 (23%)	18.8 (25%)	35.2 (23%)
DI RF	20.4	21.9	39.6
DI WF	20.4	22.0	39.7

second modes at this damage level, reducing the quality of the identified mode shapes. Furthermore, the vibration acquisitions were conducted at the end of the load cycles, under ambient vibration to a small extent, with multiple existing cracks likely closed under the structure's self-weight. In this condition, the extent of damage to the building may have a lower influence on the dynamic behaviour.

Higher MAC values (equal to or higher than 0.95) indicate that the first longitudinal mode shape remained mostly unchanged throughout Test 1, being minimally affected by the significant damage developed in the transverse walls. The first transversal mode, instead, was more affected by the damage, with a drop of its MAC to 0.83 at the end of Test 1. Nonetheless, the value remained high for the torsional mode, at 0.87, under a load application of 75%, even though the mechanism started to emerge at this load, and there was a considerable reduction in frequency for this mode, as listed in Table 10. This result suggests a relatively low sensitivity of the MAC to the damage onset and increases until significant severity. However, the direct comparison of the mode shapes may provide a deeper insight into the effect of the damage on the structure. While the undamaged building showed mainly translational vibrations in both orientations, Fig. 30 illustrates their evolution into more complex mode shapes, coupled with torsional rotations, particularly in the transverse mode. This implies rotations due to developed damage fostered by the plan irregularity. When comparing the damaged and undamaged buildings after Test 1, it can be inferred that the stiffness of the structure decreased by an average of 24%, considering the assumptions of isotropic damage. Moreover, Fig. 30; Table 11 present the extent of the correlation between the mode shapes obtained before and after the repair. The MAC values calculated by comparing DI F_T1 and DI RF show some differences, given that the former represents a damaged building with low boundary stiffness, while the latter has significantly higher boundary stiffness.

4 Conclusions

This study investigated an experimental campaign involving cyclic quasi-static and dynamic identification tests on a half-scale modern unreinforced masonry (URM) building with plan irregularity. The novelty of this research lies in being the first cyclic quasi-static test conducted on such a structure. Additionally, what further distinguishes this study is the availability of the dataset, providing valuable data for future research. While the experimental building represents a typical residential Portuguese house, similar structural configurations with plan irregularity exist in other countries. This allows the extension of the current research to a broader setting.

This research examined damage evolution, lateral strength, displacements, dynamic properties, and damage limits. Despite limitations, extensive post-processing of recorded

Table 11 MAC values at different stages

Compared Tests	1st Longitudinal	1st Transverse	1st Torsional
	MAC	MAC	MAC
DI 0 – DI 45_T1	0.96	0.91	0.91
DI 0 - DI 75_T1	0.98	0.97	0.90
DI 0 - DI F_T1	0.95	0.83	0.83
DI_F_T1 – DI RF	0.87	0.84	0.87
DI RF – DI WF	0.97	0.92	0.98

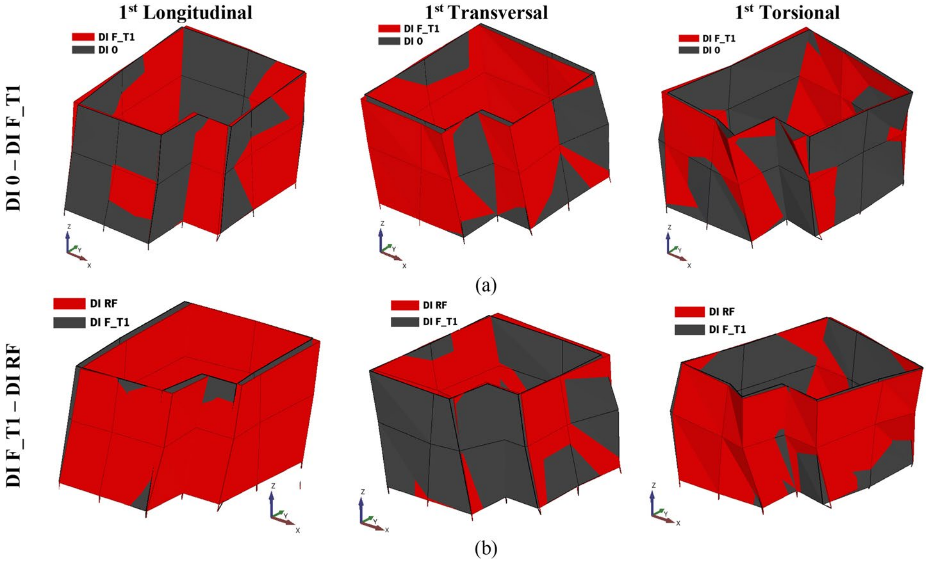

Fig. 30 Comparison of the mode shapes derived from: (**a**) DI 0 – DI F_T1, (**b**) DI F_T1 – DI RF. The mode shape amplitude factor is 1.2

data allowed for a satisfactory understanding of the structural response. The key findings are summarised as follows:

- *Cyclic behaviour and lateral strength*: The hysteretic response indicated stiffness degradation and plastic deformations, with distinct differences observed in positive and negative loading directions. Although post- peak behaviour was not fully captured, the structure reached 0.75 TBSC at 0.10% total drift before the loss of boundary restraint of the walls occurred.
- *Influence of plan irregularity*: Absolute displacement variations of up to 30% were recorded between the control points on the second floor. This highlights the critical role of node selection in defining the capacity curve. The choice of control point involves a trade-off between conservatism and capturing the structure's actual response. It is suggested that capacity curves should be derived considering multiple control points, preferably the maximum, minimum, and average of all points, and the centre of mass. Then, a comparative examination should be carried out to determine the range of the disparity and select the most representative point. Plan irregularity significantly affected displacement distribution, with torsional effects becoming more pronounced under increased lateral loading. The structure exhibited counterclockwise rotation under transverse loading, further emphasising the influence of plan irregularity.
- *Dynamic properties and stiffness degradation*: Frequency reductions of up to 25% in transverse and torsional modes were observed due to damage accumulation. Despite structural degradation, MAC values remained relatively high. That being said, dynamic identification in damaged buildings can be challenging. Once the load was released and the structure was at rest, stiffness may momentarily increase as a result of friction between the surface of the cracks and the vertical load due to crack closure.

- *Damage limits and progression*: Considerable damage occurred at very low drift values. In the positive transversal (X) direction, damage initiation was identified at 0.021% total drift (DL1), with DL2 remaining unclear. As more extensive damage evolution was defined in the negative direction, damage limits DL1, DL2, and DL3 were identified at 0.028%, 0.051%, and 0.100% total drift, respectively.
- *Effect of modifications on the structural response*: Despite the existing damage from Test 1, the boundary interface repair enabled a partial recovery of the building's stiffness. An average of 12% increase was observed in natural frequencies of the three mode shapes, indicating that the intervention was effective in improving its structural response, as this cannot be attributed only to the mass change. The building displayed significant residual strength, indicating its capacity to withstand further loading despite prior degradation. This also serves as evidence of stiffness recovery. Although Test 1 was conducted without full application of vertical loads (i.e., dead and live loads), it provides insights into the structural response and supports the continuity and completeness of the experimental investigation.

Overall, the results demonstrate that plan irregularity significantly influences deformation distribution in URM buildings. Even in a lightly damaged state, noticeable torsional effects on damage progression and capacity were observed, suggesting that these effects would be further critical as plastic damage becomes more severe. The selection of the control point influences the capacity curve definition and further implications on the performance-based assessment, despite the presence of a rigid diaphragm. Based on the observations drawn from these tests, it was decided to conduct additional experiments to achieve near-collapse conditions. This step is crucial to gain deeper insights into the ultimate capacity and failure mechanisms. The major implications of this decision and limitations in the setup require further modifications to the test setup.

Author contributions Conceptualization: Abide Aşıkoğlu, Graça Vasconcelos, Alberto Barontini, Paulo B. Lourenço; Methodology: Abide Aşıkoğlu, Graça Vasconcelos, Alberto Barontini, Paulo B. Lourenço; Formal analysis and investigation: Abide Aşıkoğlu, Alberto Barontini; Writing – original draft preparation: Abide Aşıkoğlu; Writing – review and editing: Abide Aşıkoğlu, Graça Vasconcelos, Alberto Barontini, Paulo B. Lourenço; Funding acquisition: Graça Vasconcelos, Paulo B. Lourenço; Resources: Graça Vasconcelos, Paulo B. Lourenço; Supervision: Graça Vasconcelos, Paulo B. Lourenço.

Funding This work was financially supported by FCT - Fundação para a Ciência e Tecnologia, I.P., (Grant No. PTDC/ECI-EGC/29010/2017). This work was partly financed by FCT / MCTES through national funds (PIDDAC) under the R&D Unit Institute for Sustainability and Innovation in Structural Engineering (ISISE), under reference UIDB / 04029/2020 (https://doi.org/10.54499/UIDB/04029/2020), and under the A ssociate Laboratory Advanced Production and Intelligent Systems ARISE under reference LA/P/0112/2020. Author Abide Aşıkoğlu was supported by FCT - Fundação para a Ciência e Tecnologia, I.P., by SFRH/BD/143949/2019 and COVID/BD/153438/2023 (https://doi.org/10.54499/COVID/BD/153438/2023).

Data availability The dataset generated during the current experimental campaign is available on Zenodo at the following https://doi.org/10.5281/zenodo.15096909.

Declarations

Competing interests The authors have no relevant financial or non-financial interests to disclose.

References

Adhikari RK, D'Ayala D (2020) 2015 Nepal earthquake: seismic performance and post-earthquake reconstruction of stone in mud mortar masonry buildings. Bull Earthq Eng 18:3863–3896. https://doi.org/10.1007/s10518-020-00834-y

Aldemir A, Binici B, Canbay E, Yakut A (2017) Lateral load testing of an existing two story masonry Building up to near collapse. Bull Earthq Eng 15:3365–3383. https://doi.org/10.1007/s10518-015-9821-3

Aldemir A, Binici B, Canbay E, Yakut A (2018) In situ lateral load testing of a Two-Story solid clay brick masonry Building. J Perform Constr Facil 32:04018058. https://doi.org/10.1061/(ASCE)CF.1943-5509.0001206

Ali Q, Ahmad N, Ashraf M et al (2017) Shake table tests on Single-Story Dhajji Dewari traditional buildings. Int J Architectural Herit 11:1046–1059. https://doi.org/10.1080/15583058.2017.1338789

ARTeMIS Modal v.7.0 (2023) SVS-Structural Vibration Solutions A/S

ASCE/SEI 7–16 (2017) Minimum design loads and associated criteria for buildings and other structures

Aşıkoğlu A (2024) Performance-based approach on masonry buildings by means of experimental and numerical pushover analysis. PhD Thesis. University of Minho https://hdl.handle.net/1822/92440

Aşıkoğlu A, Vasconcelos G, Lourenço PB (2021) Overview on the nonlinear static procedures and Performance-Based approach on modern unreinforced masonry buildings with structural irregularity. Buildings 11(4):147 https://doi.org/10.3390/buildings11040147

Aşıkoğlu A, Barontini A, Vasconcelos G, Lourenço P (2025) Experimental dataset on Cyclic Quasi-Static testing of a Half-. Scale Modern Unreinforced Masonry Building with Plan Irregularity https://doi.org/10.5281/zenodo.15096909

ASTM E 519–02 (2002) Standard Test Method for Diagonal Tension (Shear) in Masonry Assemblages

Athmani AE, Gouasmia A, Ferreira TM et al (2015) Seismic vulnerability assessment of historical masonry buildings located in Annaba City (Algeria) using Non ad-hoc data survey. Bull Earthq Eng 13:2283–2307. https://doi.org/10.1007/s10518-014-9717-7

Aung WY, Gautam S, Gautam D (2025) Damage mechanisms and seismic vulnerability of building structures following the 2025 M 7.7 Mandalay earthquake sequence, Myanmar. Eng Fail Anal 180. https://doi.org/10.1016/j.engfailanal.2025.109849

Avila L, Vasconcelos G, Lourenço PB (2018) Experimental seismic performance assessment of asymmetric masonry buildings. Eng Struct 155:298–314. https://doi.org/10.1016/j.engstruct.2017.10.059

Bairrão R, Silva MJF (2009) Shaking table tests of two different reinforcement techniques using polymeric grids on an asymmetric limestone full-scaled structure. Eng Struct 31:1321–1330. https://doi.org/10.1016/j.engstruct.2008.04.039

Berti M, Salvatori L, Orlando M, Spinelli P (2017) Unreinforced masonry walls with irregular opening layouts: reliability of equivalent-frame modelling for seismic vulnerability assessment. Bull Earthq Eng 15:1213–1239. https://doi.org/10.1007/s10518-016-9985-5

Beyer K, Tondelli M, Vanin F et al (2015) Seismic behaviour of unreinforced masonry buildings with reinforced concrete slabs. Assessment of in-plane and out-of-plane response

Bisch P, Carvalho E, Degee H et al (2012) Eurocode 8: seismic design of Buildings - Worked examples. European Commission Joint Research Centre, Lisbon

Bothara J, Ingham J, Dizhur D (2022) Qualifying the earthquake resilience of vernacular masonry buildings along the Himalayan Arc. J Building Eng 52. https://doi.org/10.1016/j.jobe.2022.104339

Brando G, Rapone D, Spacone E et al (2017) Damage reconnaissance of unreinforced masonry bearing wall buildings after the 2015 gorkha, nepal, earthquake. Earthq Spectra 33:S243–S273. https://doi.org/10.1193/010817EQS009M

Choudhury T, Kaushik HB (2021) Experimental evaluation of Full-Scale URM buildings strengthened using Surface-Mounted steel bands. J Struct Eng 147:1–18. https://doi.org/10.1061/(asce)st.1943-541x.0002919

Chourasia A, Bhattacharyya SK, Bhandari NM, Bhargava P (2016) Seismic performance of different masonry buildings: Full-Scale experimental study. J Perform Constr Facil 30:04016006. https://doi.org/10.1061/(ASCE)CF

Debnath P, Halder L, Chandra Dutta S (2022) Damage survey and seismic vulnerability assessment of unreinforced masonry structures in low-intensity Ambasa earthquake of Northeast India. Structures 44:372–388. https://doi.org/10.1016/j.istruc.2022.08.005

EN 1015-11 (2007) EN 1015-11:2007 Flexural and compressive strength of mortar. European Committee for Standardization (CEN)

EN 771-1 (2000) Compressive strength for masonry units. European Committee for Standardization (CEN)

EN 1015-10 (1990) Methods of test for mortar for masonry - Part 10. Determination of dry bulk density of hardened mortar. European Committee for Standardization (CEN)

EN 1052-1 (1999) Methods of test for masonry - Part 1: determination of compressive strength. European Committee for Standardization (CEN)

EN 1052-2 (1999) Methods of test for masonry - Part 2: determination of flexural strength. European Committee for Standardization (CEN)

EN 1052-3 (2002) Methods of test for masonry - Part 3: determination of initial shear strength. European Committee for Standardization (CEN)

EN 12390-3 (2019) Testing hardened concrete - Part, vol 3. Compressive strength of test specimens. European Committee for Standardization (CEN)

EN 1990:2002 + A1 (2005) Eurocode - Basis of structural design. European Committee for Standardization (CEN)

EN 1991-1-1 (2002) Eurocode 1: actions on structures - Part 1–1: general actions - Densities, self-weight, imposed loads for buildings. European Committee for Standardization (CEN)

EN 1996-1-1:2005 (2005) Eurocode 6: design of masonry structures: part 1–1. General rules for reinforced and unreinforced masonry structures (CEN)

EN 1998-1:2004 (2004) Eurocode 8: design of structures for earthquake resistance – Part 1: general rules, seismic actions and rules for buildings. European Committee for Standardization (CEN)

Esposito R, Messali F, Ravenshorst GJP et al (2019) Seismic assessment of a lab-tested two-storey unreinforced masonry Dutch terraced house. Bull Earthq Eng 17:4601–4623. https://doi.org/10.1007/s10518-019-00572-w

Ewins D (2000) Modal testing: theory, practice, and application. Research Studies Press LTD., England

Gattesco N, Rizzi E, Boem I et al (2023) Full-scale Cyclic tests on a stone masonry Building to investigate the effectiveness of a one-side application of the composite reinforced mortar system. Eng Struct. 296: https://doi.org/10.1016/j.engstruct.2023.116967

Gautam D, Fabbrocino G, Santucci de Magistris F (2018) Derive empirical fragility functions for Nepali residential buildings. Eng Struct 171:617–628. https://doi.org/10.1016/j.engstruct.2018.06.018

Giordano N, De Luca F, Sextos A (2021) Analytical fragility curves for masonry school Building portfolios in Nepal. Bull Earthq Eng 19:1121–1150. https://doi.org/10.1007/s10518-020-00989-8

Graziotti F, Tomassetti U, Kallioras S et al (2017) Shaking table test on a full scale URM cavity wall Building. Bull Earthq Eng 15:5329–5364. https://doi.org/10.1007/s10518-017-0185-8

Grünthal G (1998) European macroseismic scale 1998 : EMS-98. European seismological commission, subcommission on engineering seismology. Working Group Macroseismic scales

Haindl M, Smith IFC, Beyer K (2024) A database of shake-table tests conducted on unreinforced masonry buildings. Earthq Spectra. https://doi.org/10.1177/87552930241268214

Halder L, Chandra Dutta S, Sharma RP (2020) Damage study and seismic vulnerability assessment of existing masonry buildings in Northeast India. J Building Eng 29. https://doi.org/10.1016/j.jobe.2020.101190

Imtiaz A, Saloustros S, Beqiraj M et al (2025) Understanding Building damage through the lens of the Swiss post-seismic reconnaissance mission of 2023 al haouz, morocco, earthquake. Sci Rep 15. https://doi.org/10.1038/s41598-025-00659-2

Kallioras S, Guerrini G, Tomassetti U et al (2018) Experimental seismic performance of a full-scale unreinforced clay-masonry Building with flexible timber diaphragms. Eng Struct 161:231–249. https://doi.org/10.1016/j.engstruct.2018.02.016

Kallioras S, Correia AA, Graziotti F et al (2020) Collapse shake-table testing of a clay-URM Building with chimneys. Bull Earthq Eng 18:1009–1048. https://doi.org/10.1007/s10518-019-00730-0

Korswagen PA (2024) Quantifying the probability of light damage to masonry structures: an exploration of crack initiation and progression due to seismic vibrations on masonry buildings with existing damage. PhD Thesis. Delft University of Technology

Lagomarsino S, Cattari S (2015) PERPETUATE guidelines for seismic performance-based assessment of cultural heritage masonry structures. Bull Earthq Eng 13:13–47. https://doi.org/10.1007/s10518-014-9674-1

Lourenço PB, Marques R (2020) Design of masonry structures (General rules): highlights of the new European masonry code. In: Kubica, Kwiecien B (ed) Brick and block masonry - From historical to sustainable masonry. Taylor & Francis, Krakow

Lourenço PB, Avila L, Vasconcelos G et al (2013) Experimental investigation on the seismic performance of masonry buildings using shaking table testing. Bull Earthq Eng 11:1157–1190. https://doi.org/10.1007/s10518-012-9410-7

Magenes G, Calvi GM, Kingsley G (1995) Seismic testing of a Full-scale. Test Procedure and Measured Experimental Response, Two-story Masonry Building

Magenes G, Penna A, Senaldi IE et al (2014) Shaking table test of a strengthened full-scale stone masonry Building with flexible diaphragms. Int J Architectural Herit 8:349–375. https://doi.org/10.1080/15583058.2013.826299

Mercimek Ö (2023) Seismic failure modes of masonry structures exposed to Kahramanmaraş earthquakes (Mw 7.7 and 7.6) on February 6, 2023. Eng Fail Anal 151.https://doi.org/10.1016/j.engfailanal.2023.107422

Morandi P, Albanesi L, Graziotti F et al (2018) Development of a dataset on the in-plane experimental response of URM piers with bricks and blocks. Constr Build Mater 190:593–611. https://doi.org/10.1016/j.conbuildmat.2018.09.070

NTC (2018) Norme tecniche per Le costruzioni. DM 17/1/2018. Gazzetta Ufficiale della Repubblica Italiana

Parisi F, Augenti N (2013) Seismic capacity of irregular unreinforced masonry walls with openings. Earthq Eng Struct Dyn 42:101–121. https://doi.org/10.1002/eqe.2195

Shahzada K, Khan AN, Elnashai AS et al (2012) Experimental seismic performance evaluation of unreinforced brick masonry buildings. Earthq Spectra 28:1269–1290. https://doi.org/10.1193/1.4000073

Singh Y, Lang DH, Prasad J, Deoliya R (2013) An analytical study on the seismic vulnerability of masonry buildings in India. J Earthquake Eng 17:399–422. https://doi.org/10.1080/13632469.2012.746210

TBSC (2019) Turkish Building Seismic Code

Triller P, Tomaževič M, Gams M (2019) Seismic strengthening of clay block masonry Buildings with composites: an experimental study of a full scale three-storey Building model. Bull Earthq Eng 17:4049–4080. https://doi.org/10.1007/s10518-019-00609-0

Vanin F, Zaganelli D, Penna A, Beyer K (2017) Estimates for the stiffness, strength and drift capacity of stone masonry walls based on 123 quasi-static Cyclic tests reported in the literature. Bull Earthq Eng 15:5435–5479. https://doi.org/10.1007/s10518-017-0188-5

Yi T, Moon FL, Leon RT, Kahn LF (2006) Lateral load tests on a two-story unreinforced masonry building. Journal of Structural Engineering 132:643–652. https://doi.org/10.1061/(ASCE)0733-9445